Ocean Engineering 228 (2021) 108853

Contents lists available at ScienceDirect

Ocean Engineering

journal homepage: www.elsevier.com/locate/oceaneng

A 2D+t approach for the transverse viscous loads in a modular maneuvering model

Øyvind Rabliås *, Trygve Kristiansen

Department of Marine Technology, NTNU, 7491, Trondheim, Norway

ARTICLE INFO

Keywords:
Maneuvering in waves
Turning circle
Transverse viscous loads
2D+t
Cross-flow
Duisburg test case

ABSTRACT

The importance of the transverse viscous loads, in a modular maneuvering model, is investigated. A method to estimate steady sectional drag coefficients is first presented. A 2D+t approach, which accounts for forward-speed effects, is also presented. The time-varying drag coefficients, in the 2D+t method, are estimated with three methods: two simplified methods using results from the literature directly, and one more sophisticated method which uses time-derivatives, from time-dependent drag coefficients for hull forms in the literature, and integrates the drag coefficients along the hull. Turning circles with 25° and 35° rudder angle are simulated in calm water and regular waves for a range of wavelengths between $\lambda/L_{pp} = 0.281$ and 1.120, with wave steepness $H/\lambda = 1/40$, and initial head sea. The Duisburg Test Case (DTC) is used as a test ship. The numerical simulations are compared with free-running model tests. Overall, the 2D+t method, with integrated drag coefficients, shows a better match with the experiments compared to the cross-flow approach. However, both methods capture the main trends considering tactical diameter and advance for the tested wave conditions. Furthermore, using scaled time-varying drag coefficients for a circular cylinder can be a good starting point in a 2D+t approach.

1. Introduction

Maneuvering behavior of ships has been investigated for decades. Regression models, also referred to as Abkowitz models, and modular models are the two dominating mathematical models for ship maneuvering. Traditionally regression models have been the most popular mathematical model for maneuvering simulations (Sutulo and Soares, 2011).

In a regression model, the mathematical model is constructed from hull coefficients obtained from experimental tests or numerical simulations. Planar motion mechanism (PMM) tests have typically been applied to obtain the coefficients. These tests are usually done in calm water, but they can also be done in waves. As computational speed has been rapidly increasing, such tests can now be done virtually with CFD. During a maneuvering simulation, these coefficients are considered to be tabulated values, which means that regression models are suitable for real-time simulations.

The lack of physical meaning can be a drawback of regression models (Hooft, 1994). This makes it difficult to compare different ships concerning maneuvering behavior and to get a thorough understanding of the physical phenomena involved. Another drawback is that the computation of the maneuvering coefficients can be complicated and time-intensive.

A modular approach, solver-in-the-loop, is an alternative model which can give accurate results (Sutulo and Soares, 2011). In a modular model, the different physical phenomena are calculated separately. Maneuvering Modeling Group (MMG) models, as presented by Ogawa et al. (1977) and Yasukawa and Yoshimura (2015), are examples of modular maneuvering models.

Sutulo and Soares (2019) emphasize the importance of having accurate maneuvering models, which can be used in the design stage. It is especially important with maneuvering models with minimal tuning. Empirical methods are often used in this context. However, results in Sutulo and Soares (2019) demonstrated that few empirical maneuvering models were capable to predict, fairly accurate compared to experiments, the main measures of a turning circle in calm water. For some of the empirical methods, the tactical diameter was more than 50% higher than the experimental results.

Simulations with modular models can clarify which physical phenomena that dominate in different type of maneuvers. Sensitivity studies show that the transverse viscous loads are of significant importance in a turning circle with 35° rudder angle. These loads are often calculated according to the cross-flow principle, which neglects the effect of forward speed. The resulting sway force and yaw moment are strongly dependent on the sectional drag coefficients. The method is often

* Corresponding author.
E-mail address: oyvind.rablias@ntnu.no (Ø. Rabliås).

https://doi.org/10.1016/j.oceaneng.2021.108853
Received 30 August 2020; Received in revised form 5 March 2021; Accepted 6 March 2021
Available online 10 April 2021

Nomenclature

A_R	[m^2] Rudder area
B	[m] Beam of the ship
C_B	[–] Block coefficient
C_D	[–] Drag coefficient
C_{D_0}	[–] Rudder surface friction coefficient
$C_{D,\infty}$	[–] Steady drag coefficient
$C_D(t')$	[–] Time-varying drag coefficient
$C_D^*(t')$	[–] Time-integrated drag coefficient
C_F	[–] Frictional resistance coefficient
C_L	[–] Lift coefficient
C_T	[–] Total resistance coefficient
C_{th}	[–] Propeller thrust loading coefficient
C_{TN}	[–] Reduction coefficient
d	[m] Ship draft
D_p	[m] Propeller diameter
Fn	[–] Froude number
GM	[m] Metacentric height
H	[m] Wave height
I_{44}	[kgm^2] Roll moment of inertia
I_{66}	[kgm^2] Yaw moment of inertia
I_{46}, I_{64}	[kgm^2] Coupled roll–yaw and yaw–roll moment of inertia
k	[m^{-1}] Wave number
KC	[–] Keulegan–Carpenter number
KG	[m] Height of ship's center of gravity above keel
k_m	[–] Rudder velocity coefficient
K_T	[–] Propeller thrust coefficient
K_R, K_{PROP}	[Nm] Roll moments in body-fixed coordinate system due to rudder, and propulsion
L_{bk}	[m] Length of bilge keel segments
L_{pp}	[m] Length between perpendiculars
n	[s^{-1}] Number of propeller revolutions per second
N_R, N_{PROP}, N_{CF}	[Nm] Yaw moments in body-fixed coordinate system due to rudder, propulsion, and transverse viscous loads
$Oxyz$	Cartesian right-handed body-fixed coordinate system
$OX_0Y_0Z_0$	Earth-fixed Cartesian right-handed coordinate system
p, r	[rad/s] Roll- and yaw-rate in body-fixed coordinate system
r_b	[m] Bilge radius
R_F	[N] Frictional resistance
Re	[–] Reynolds number
R_W	[N] Wave-making resistance
R_T	[N] Calm water ship resistance
$\overline{R}_X, \overline{R}_Y, \overline{R}_N$	Second order mean loads due to regular waves
$\overline{R}_{X,1}$	Added resistance due to linear wave-induced motions
$\overline{R}_{X,2}$	Added resistance due to wave reflection
s	[m] Distance a section has moved transversely
S	[m^2] Wetted surface of hull
t	[–] Thrust deduction factor
T	[s] Wave period
$T(J)$	[N] Propeller thrust as a function of propeller advance number
t'	Non-dimensional time (or displacement)
U_A	[m/s] Propeller inflow velocity
u, v	[m/s] Surge and sway velocity in body-fixed coordinate system
u_r, v_r	[m/s] Longitudinal and transverse component of inflow velocity to the rudder
x_G, y_G, z_G	[m] Center of gravity in body-fixed coordinate system
x_R	[m] x-position of rudder in body-fixed coordinate system
X_R, X_{PROP}	[N] Forces in x-direction in body-fixed coordinate system due to rudder, and propulsion
Y_R, Y_{PROP}, Y_{CF}	[N] Forces in y-direction in body-fixed coordinate system due to rudder, propulsion, and transverse viscous loads
Y_{PT}, N_{PT}	Factors to estimate propeller lateral loads
$2D + t^0$	2D+t approach where time-varying drag coefficients are scaled directly from the literature
$2D + t^{cyl}$	2D+t approach where scaled time-varying drag coefficients for a circular cylinder are applied
α	[deg] Drift angle
β_0	[deg] Wave heading
β_R	[deg] Angle of mean inflow to rudder
δ	[deg] Rudder angle
Δ	[4kg] Displacement mass
ζ_A	[m] Wave amplitude
Λ	[–] Rudder aspect ratio
λ	[m] Wavelength
ν	[m^2/s] Kinematic viscosity of water
ρ	[kg/m^3] Density of water
ϕ, ψ	[deg] Roll- and yaw-rotation in body-fixed coordinate system
Φ, Ψ	[deg] Roll- and yaw-rotation in Earth-fixed coordinate system
ω	[rad/s] Angular wave frequency

further simplified, by setting the drag coefficient to be constant along the hull. The argument behind such simplification is that cross-flow is a very approximate model and more realistic drag coefficients will not necessarily improve the results (Sutulo and Soares, 2011). Shen (2018) presented a pragmatic method to estimate sectional drag coefficients. Ship sections were simplified to similar geometries, and corrections for important parameters were applied, such as free-surface effects, bilge radius, and 3D-effects. The calculated transverse viscous force agrees well with model tests (Shen, 2018).

There are several, more sophisticated methods to calculate the transverse viscous loads. Landrini and Campana (1996) investigated a simplified geometry, a flat plate with steady drift and during a steady turn. The separation at the ship keel was modeled with a vortex-sheet method. For a simplified geometry, as a flat plate, where the separation point is known, this approach may be appropriate. However, for realistic hull shapes where the separation point is unknown, the separation point must be determined. Aarsnes (1984) calculated also the transverse viscous loads with a vortex-sheet method. He investigated realistic ship sections, where the separation points were determined by boundary layer calculations. Yeung et al. (2008) proposed a new method to calculate the transverse viscous loads with forward speed effects included. They combined the Free Surface Random Vortex Method (FSRVM) with slender body theory. The estimated transverse loads showed good agreement with experimental results.

Solving the Navier–Stokes equations, with CFD, in principle provides you the hydrodynamic loads, including the transverse viscous loads. Traditionally, the computational time has been a disadvantage with CFD. However, lately CFD has become more and more manageable, especially for 2D problems. Arslan et al. (2016) investigated the flow around ship sections. The calculated steady drag coefficients were in good compliance with experimental results. Cura-Hochbaum and Uharek (2016) and Chillcce and el Moctar (2018) used a regression model to perform turning circles in calm water and regular waves. The maneuvering coefficients were obtained from PMM tests performed with CFD. The results were in good agreement with experimental results, hence it is natural to believe that the transverse loads were estimated satisfactorily.

CFD calculations should be handled with care, especially mesh generation and turbulence models need special attention. Great knowledge about the physics of these topics are needed to obtain accurate results. This can be recognized in a benchmark study by Shigunov et al. (2018), where CFD methods showed great potential but could also deliver erratic results. If CFD is used to calculate the transverse viscous loads in a modular model, you will also obtain non-viscous loads. Meaning that you need to subtract the loads which are estimated by other modules, e.g. potential lifting loads.

Common for the methods mentioned above, is that quite some effort is needed to implement these methods. Furthermore, time-domain simulations are needed to obtain the transverse viscous loads. In a modular maneuvering model, where the transverse viscous loads is only one of many modules, the effort of implementing these methods can often be considered to be too much. This is probably the reason that the approximate cross-flow approach is the dominant method in modular maneuvering models.

Chapman (1975) introduced a strip-theory to calculate the transverse viscous loads, which accounts for forward speed effects, the 2D+t theory. Faltinsen (2005) exemplified this theory in a maneuvering context, to calculate the non-linear transverse viscous loads on a circular cylinder with constant diameter. Ommani et al. (2012) implemented the theory for a vessel on a straight course with a drift angle. They simplified the cross-sections into half circles with radius equal to the ship sections draft. For circular cylinders there exist experimental and numerical results for start-up flows in the literature. The estimated sway force agreed well with experiments, while there was more discrepancies for the yaw moment. Ommani and Faltinsen (2014) investigated the same problem with transient drag coefficients calculated with a 2D Navier–Stokes solver, which captures the flow separation of the actual ship shape. The results showed a good agreement with experimental results. The transverse viscous loads were significantly higher than the loads calculated with the simplified method in Ommani et al. (2012). Moreover, the 2D Navier–Stokes solver captured the transverse force distribution at the bow better than when the geometry was simplified to a circular cylinder. This is of high importance in calculating the yaw moment.

Alsos and Faltinsen (2018) generalized the 2D+t method in Faltinsen (2005), to account for all six rigid-body degrees of freedom. They investigated a dropped circular cylinder, with a blunt front, which can be compared to a generalized maneuvering problem. However, there is no one, in the authors' knowledge, that has implemented the 2D+t theory in a classical maneuvering problem.

In the present work, a modular maneuvering model for maneuvering in waves is presented based on slender-body theory for the still water part, and strip theory to account for the waves. The mathematical model is based on Skejic (2008), i.e. a two-time scale model, with some modifications. The model is within the framework of real-time simulation, and all loads can be computed in the loop. Special attention is given to the transverse viscous loads, which are of significant importance in a tight turn. Following the approach in Shen (2018), the steady sectional drag coefficients are calculated pragmatically based on drag coefficients in the literature. Furthermore, a 2D+t theory, based on Faltinsen (2005) and Alsos and Faltinsen (2018), is implemented in the maneuvering model. Three methods are presented to calculate the time-varying drag coefficient; one by scaling time-varying drag coefficients for a range of relevant geometries from Aarsnes (1984), one by scaling the time-varying drag coefficient for a circular cylinder, while the last method time-integrates $\frac{dC_D(t')}{dt'}$ with time-derivatives estimated from Aarsnes (1984). The first two methods are very simplified methods using results from the literature directly, while the latter is a more sophisticated method. The features of these three methods will be discussed. The *Duisburg Test Case* (DTC) is used as a test ship. Turning circles with 35° and 25° rudder angel, in calm water and regular waves, are compared with experimental results from Rabliås and Kristiansen (2019).

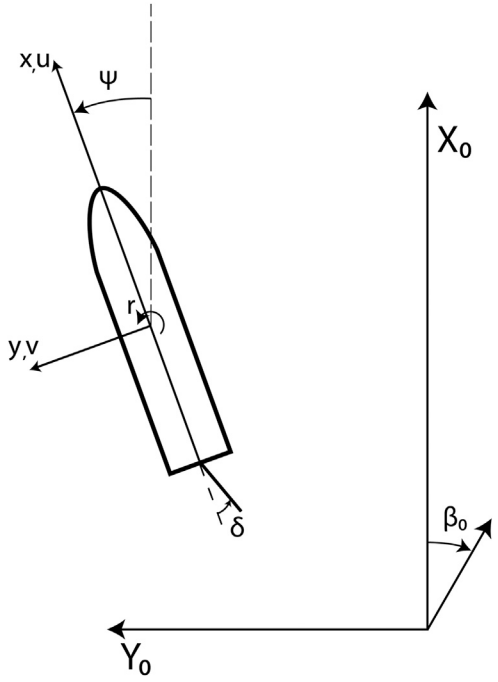

Fig. 1. Body-fixed coordinate system xyz and Earth-fixed coordinate system $X_0Y_0Z_0$. Positive direction of yaw Ψ, yaw-rate r, rudder angle δ, and wave heading β_0 are indicated.

2. Numerical formulation

2.1. Mathematical model

A right-handed body-fixed coordinate system, xyz, with the z-axis pointing upwards through the center of gravity, with $z = 0$ at calm water level is applied. The Earth-fixed coordinate system $X_0Y_0Z_0$ is a right-handed coordinate system with Z_0-axis pointing upwards. Both coordinate systems with definitions and positive rotations are given in Fig. 1.

The mathematical model is based on the maneuvering model by Skejic (2008), which is a modified version of the 3-DOF slender body theory by Söding (1982). The 4-DOF maneuvering equations implemented in the current model are given in Eq. (1). An explanation of the different modules and the terms in Eq. (1) follows.

The left-hand side of Eq. (1) represents inertia terms in the surge–sway–roll–yaw equations of motions for a rigid body in the body-fixed coordinate system given in Fig. 1. The right-hand side represents the hydrodynamic loads acting on the hull.

$X_{\dot{u}}$, $Y_{\dot{v}}$, $Y_{\dot{p}}$, $Y_{\dot{r}}$, $K_{\dot{v}}$, $K_{\dot{p}}$, $K_{\dot{r}}$, $N_{\dot{v}}$, $N_{\dot{p}}$, $N_{\dot{r}}$, Y_v, Y_p, Y_r, K_v, K_p, K_r, N_v, N_p, and N_r are the so-called maneuvering coefficients. The zero-frequency added mass terms $X_{\dot{u}}$, $Y_{\dot{v}}$, $Y_{\dot{p}}$, $Y_{\dot{r}}$, $K_{\dot{v}}$, $K_{\dot{p}}$, $K_{\dot{r}}$, $N_{\dot{v}}$, $N_{\dot{p}}$, and $N_{\dot{r}}$ are

$$\begin{bmatrix} M & 0 & 0 & 0 \\ 0 & M & 0 & 0 \\ 0 & 0 & I_{44} & -I_{46} \\ 0 & 0 & -I_{64} & -I_{66} \end{bmatrix} \begin{bmatrix} \dot{u} \\ \dot{v} \\ \dot{p} \\ \dot{r} \end{bmatrix} + \begin{bmatrix} 0 & -Mr & 0 & 0 \\ 0 & 0 & 0 & Mu \\ 0 & 0 & 0 & 0 \\ 0 & 0 & 0 & 0 \end{bmatrix} \begin{bmatrix} u \\ v \\ p \\ r \end{bmatrix} = \begin{bmatrix} X_{\dot{u}} & 0 & 0 & 0 \\ 0 & Y_{\dot{v}} & Y_{\dot{p}} & Y_{\dot{r}} \\ 0 & K_{\dot{v}} & K_{\dot{p}} & K_{\dot{r}} \\ 0 & N_{\dot{v}} & N_{\dot{p}} & N_{\dot{r}} \end{bmatrix} \begin{bmatrix} \dot{u} \\ \dot{v} \\ \dot{p} \\ \dot{r} \end{bmatrix} + \begin{bmatrix} 0 & -C_{TN}Y_{\dot{v}}r & -Y_{\dot{p}}r & -Y_{\dot{r}}r \\ 0 & 0 & 0 & X_{\dot{u}}u \\ 0 & 0 & 0 & 0 \\ 0 & -X_{\dot{u}}u & 0 & 0 \end{bmatrix} \begin{bmatrix} u \\ v \\ p \\ r \end{bmatrix}$$
$$+ \begin{bmatrix} 0 & 0 & 0 & 0 \\ 0 & Y_v & Y_p & Y_r \\ 0 & K_v & K_p & K_r \\ 0 & N_v & N_p & N_r \end{bmatrix} \begin{bmatrix} u \\ v \\ p \\ r \end{bmatrix} - \begin{bmatrix} 0 & 0 & 0 & 0 \\ 0 & 0 & 0 & 0 \\ 0 & 0 & C_{44} & 0 \\ 0 & 0 & 0 & 0 \end{bmatrix} \begin{bmatrix} \int_0^t u dt \\ \int_0^t (v + z_G p + u\psi) dt \\ \phi \\ \psi \end{bmatrix} + \begin{bmatrix} X_R \\ Y_R \\ K_R \\ N_R \end{bmatrix} + \begin{bmatrix} X_{PROP} \\ Y_{PROP} \\ K_{PROP} \\ N_{PROP} \end{bmatrix} + \begin{bmatrix} X_{CF} \\ Y_{CF} \\ K_{CF} \\ N_{CF} \end{bmatrix} + \begin{bmatrix} \overline{R}_X \\ \overline{R}_Y \\ \overline{R}_K \\ \overline{R}_N \end{bmatrix} \tag{1}$$

calculated with the 3D panel code WAMIT. The rest of the maneuvering coefficients, the lifting terms, are calculated according to Söding (1982). In Söding (1982), the lifting coefficients are constructed from zero frequency 2D added mass coefficients. In the present work, these 2D added mass coefficients are calculated with a 2D boundary element code.

The term $-C_{TN}Y_{\dot{v}}rv$ represents the longitudinal component of the centrifugal force, which gives an important contribution to speed loss in a turn, where C_{TN} is an empirical constant between 0.2 and 0.8 (Skejic, 2008; Artyszuk, 2003). In the present work, C_{TN} is set to 0.5. Subscript R, PROP, and CF represent Rudder forces, propulsion forces, and viscous loads due to flow separation. $\overline{R}$ represents the mean drift loads from regular waves. The modular approach allows us to calculate the calm water hydrodynamic loads separately in a quasi-steady manner (Yasukawa and Yoshimura, 2015). According to the two time-scale assumption the second order mean wave loads follows a more slowly varying time scale, and they are updated in a separate module with input parameters (velocity and heading) obtained from the maneuvering module. Propulsion, rudder, and drift loads are estimated by conventional methods, while we present new models for the transverse viscous loads.

Following the Euler transformation derived in Faltinsen (2005), the relation between the ship position in the body-fixed coordinate-system (x, y, x) and the Earth-fixed coordinate-system (X_0, Y_0, Z_0) can be written as:

$$\begin{aligned} \frac{dX_0}{dt} &= u\cos\psi - v\cos\Phi\sin\psi \\ \frac{dY_0}{dt} &= u\sin\psi + v\cos\Phi\cos\psi \\ \frac{d\Phi}{dt} &= p \\ \frac{d\psi}{dt} &= r\cos\Phi \end{aligned} \tag{2}$$

where u, v, p, r, ϕ, and ψ are the surge velocity, sway velocity, roll-rate, yaw-rate, roll angle, and yaw angle in the body-fixed coordinate-system (x, y, x). X_0, Y_0, Φ, and Ψ are the x-position, y-position, roll angle, and yaw angle in the global coordinate-system.

Time integration of the equation system (1)–(2) is performed with a fourth-order Runge–Kutta scheme. All time-varying loads and coefficients, except the second order mean wave loads, are updated at each sub-step of the time integration. The second order mean wave loads are assumed to have a different time scale and they are updated at a different time scale. The second order mean loads are updated at a predetermined threshold for heading and velocity. Based on a convergence study, where the threshold was systematically varied, the threshold is set to $\Delta\Psi = 2°$ and $\Delta u = 0.2$ m/s (full scale).

2.2. Resistance and propulsion module

The resulting longitudinal force of the propeller thrust and the calm water resistance is

$$X_{PROP} = -R_T(u) + (1-t)T(J) \tag{3}$$

where $R_T(u)$ is the calm water resistance for a given velocity, t is the thrust deduction factor, and $T(J)$ is the propeller thrust for a given propeller advance number, J. The propeller thrust can also be expressed with a non-dimensional parameter K_T,

$$K_T(J) = \frac{T(J)}{\rho n^2 D_p^4} \tag{4}$$

where n is the number of propeller revolutions per second, ρ is the density of water, and D_p is the propeller diameter. Experimental K_T values for the DTC hull, obtained from el Moctar et al. (2012), are used in the present work. Vessels equipped with single-screw propellers will experience a lateral force and yaw moment from the propeller, Y_{PROP}, and N_{PROP}. These lateral loads are in general small, and they are often neglected (Tello Ruiz, 2018). However, some authors account for the lateral propeller loads. Oltmann and Sharma (1984) propose to represent the lateral propeller force with the constants Y_{PT} and N_{PT}, such that

$$\begin{aligned} Y_{PROP} &= Y_{PT}T(J) \\ N_{PROP} &= N_{PT}T(J) \end{aligned} \tag{5}$$

Wave-making resistance R_W and frictional resistance R_F are the two dominating contributions to the calm water resistance. The calm water resistance can be approximated as

$$R_T \cong R_W + R_F(1+k) \tag{6}$$

where k is the so-called form factor. The calm water resistance can also be written on non-dimensional form:

$$C_T = \frac{R_T}{0.5\rho S U^2} \tag{7}$$

where S is the wetted surface of the hull, and U is the forward speed. Experimental values of the wave-making resistance coefficient $C_W = \frac{R_W}{0.5\rho S U^2}$, for the DTC hull, are obtained from Shigunov et al. (2018), while the frictional resistance coefficient C_F is calculated according to the ITTC friction line

$$C_F = \frac{0.075}{(\log Re - 2)^2} = \frac{R_F}{0.5\rho S U^2} \tag{8}$$

where Re is the Reynolds number, $Re = \frac{U L_{pp}}{\nu}$.

2.3. Rudder module

A conventional rudder model is applied, where the rudder induced forces and moments, in the body-fixed coordinate-system, are

$$\begin{aligned} X_R &= L\sin\beta_R - D\cos\beta_R \\ Y_R &= L\cos\beta_R + D\sin\beta_R \\ N_R &= x_R Y_R \end{aligned} \tag{9}$$

where $\beta_R = \tan^{-1}(-v_r/u_r)$, and u_r and v_r are the longitudinal and transverse component of the ambient inflow velocity to the rudder.

$$\begin{aligned} u_r &= U_A[1 + k_m(\sqrt{1 + C_{th}} - 1)] \\ v_r &= v + x_R r \end{aligned} \tag{10}$$

$U_A = U(1-w)$ is the propeller inflow velocity, where w is the wake fraction and U the forward speed, $C_{th} = \frac{T(J)}{0.5\rho U_A^2 \pi D_p^2/4}$ is the propeller thrust loading coefficient. k_m accounts for the distance-to-propeller diameter ratio, x_d/D_p, where x_d is the distance between the propeller and rudder. This coefficient is between 0.5 and 1, where $k_m = 0.5$ and $k_m = 1$ corresponds to distance-to-propeller diameter ratio 0 and ∞ respectively. In the present work $k_m = 0.55$. L and D are the rudder lift and drag, their definitions are given by

$$\begin{aligned} L &= 0.5 C_L \rho A_R (u_r^2 + v_r^2) \\ D &= 0.5 C_D \rho A_R (u_r^2 + v_r^2) \end{aligned} \tag{11}$$

A_R is the rudder area. The lift and drag coefficients, C_L and C_D, are calculated according to Bertram (2000).

$$\begin{aligned} C_L &= 2\pi \frac{\Lambda(\Lambda+0.7)}{(\Lambda+1.7)^2} \sin\alpha + C_Q \sin\alpha |\sin\alpha| \cos\alpha \\ C_D &= \frac{C_L^2}{\pi\Lambda} + C_Q |\sin\alpha|^3 + C_{D_0} \end{aligned} \tag{12}$$

where Λ is the rudder aspect ratio, C_Q is the resistance coefficient (≈ 1), $\alpha = \delta + \beta_R$ is the angle of attack where δ is the rudder angle, and $C_{D_0} = 2.5\frac{0.075}{(\log Re - 2)^2}$ represents the rudder surface friction.

2.4. Mean 2nd order drift loads

The mean second order wave loads are calculated according to Faltinsen et al. (1980). Mean second order drift forces in $x-$ and y-direction, $\overline{R}_X$ and $\overline{R}_Y$, and the mean second order yaw moment $\overline{R}_N$ are accounted for. For relative wavelengths approximately above $\lambda/L \geq 0.5$, the drift loads are dominated by the ship motions. In this range of wavelengths, the second order drift loads are calculated by the pressure integration method by Faltinsen et al. (1980). For shorter wavelengths, the drift loads are dominated by wave reflections from the ship hull. In this range of wavelengths the drift loads are calculated with the asymptotic theory for asymptotic short wavelengths (Faltinsen et al., 1980). Both the pressure integration method and the asymptotic method for short waves are derived with forward speed. The classical STF-strip theory (Salvesen et al., 1970) is applied to calculate the linear wave-induced ship motions. The 2D radiation problems, for every ship section, are solved with a 2D boundary element method. Roll damping is accounted for with the procedure by Ikeda et al. (1978), Ikeda (2004).

There is no sharp transition between these two regimes, for some wavelengths both ship motions and wave reflection will contribute to the second order drift loads. Fujii (1975) proposed a function which combines added resistance calculated from ship motions methods and wave reflection methods:

$$R = \frac{\pi I_1(kd)}{\sqrt{\pi^2 [I_1(kd)]^2 + [K_1(kd)]^2}} \tag{13}$$

I_1 is the modified Bessel function of the first kind, K_1 is the modified Bessel function of the second kind, k is the wave number, and d is the ship draft. According to Fujii (1975) the added resistance can now be written as

$$\overline{R}_X = \overline{R}_{X,1} + R^2 \overline{R}_{X,2} \tag{14}$$

where $\overline{R}_{X,1}$ is the added resistance calculated with pressure integration and $\overline{R}_{X,2}$ is the added resistance calculated with asymptotic theory for short waves.

To ensure that the added resistance is calculated purely by the asymptotic method for short waves and purely with pressure integration for the longest wave, the expression by Fujii (1975) is slightly adjusted. In the present work, the added resistance is calculated according to Eq. (15).

$$\overline{R}_X = (1 - R^2)\overline{R}_{X,1} + R^2 \overline{R}_{X,2} \tag{15}$$

The interpretation in Eq. (15) is used by other authors, e.g. Guo and Steen (2010). Eq. (15) is also applied for the mean second order sway force and yaw moment.

Applying equation (15) for the DTC hull, we find that the second order drift loads are mainly calculated according to the pressure integration method for relative wavelengths, λ/L_{pp}, above approximately 0.6.

In Fig. 2 added resistance in head and following waves, with forward speed corresponding to Froude number Fn = 0.052 and Fn = 0.14, where Fn = $\frac{U}{\sqrt{gL_{pp}}}$, are compared with experimental results in Sprenger and Fathi (2015). In head waves there is acceptable agreement with the experiments. The largest deviation can be found in the short wave range. This is a range where the added resistance is calculated by a combination of the pressure integration method and the asymptotic method for short waves, and the asymptotic method dominates more and more when the wavelength decreases. Moreover, there is an outlier in the experimental result, in head sea with Froude number 0.052, which not are captured by the numerical results. In following waves, the results deviates more from the experiments. For Froude number 0.14, the added resistance is significantly overestimated for long waves, while there is better match for the shorter waves. For Froude number 0.052, the experiments shows an added thrust, which is not captured by the present method.

Mean drift loads with Froude number 0.052 in oblique head and oblique following sea, wave headings 120° and 60°, are presented in Fig. 3. For R_X, we can observe the same trend as for Froude number 0.14, that the added resistance has an acceptable match with experiments for oblique head waves, while there are larger discrepancies for oblique following waves. For the y-drift and yaw-drift, the main trends are captured, but there is a significant deviation from the experiments for some wavelengths.

It is expected that the discrepancies in mean drift loads will affect the maneuvering behavior for those conditions. The added resistance is in general not predicted well in following and oblique following waves, which will influence the forward speed during a turning maneuver. Furthermore, for some wavelengths the discrepancies in R_Y and R_N are relatively large. It is expected that, in particular the yaw-drift, has a significant importance in a turning maneuver (Wicaksono and Kashiwagi, 2018). Moreover, we acknowledge the challenges in measuring the mean loads experimentally, which also contribute to the discrepancies.

2.5. Transverse viscous loads

Until now, we have referred to methods based on other authors' work, that we apply in our modular maneuvering model. In the present section, we describe different models that we have developed in order to improve the physical representation of the transverse, viscous loads. One method based on the cross-flow assumption, and three methods based on the 2D+t theory are proposed. Results from sensitivity studies will be presented later.

2.5.1. Cross-flow formulation

For large drift angles, the nonlinear viscous loads due to flow separation from the ship hull, typically the ship keel, can be calculated according to the cross-flow principle, where interaction between strips along the hull is neglected. The surge force due to flow separation, X_{CF}, is neglected, while that in sway, Y_{CF}, and yaw, N_{CF}, are calculated according to

$$Y_{CF} = -0.5\rho \int_L \{C_D(x)(v + xr)|v + xr|d(x)\}dx \tag{16}$$

$$N_{CF} = -0.5\rho \int_L \{C_D(x)x(v + xr)|v + xr|d(x)\}dx \tag{17}$$

$C_D(x)$ is the sectional drag coefficient, $d(x)$ is the sectional still water draft, v and r are the sway velocity and yaw-rate in the body-fixed coordinate-system, and x is the $x-$coordinate of the section.

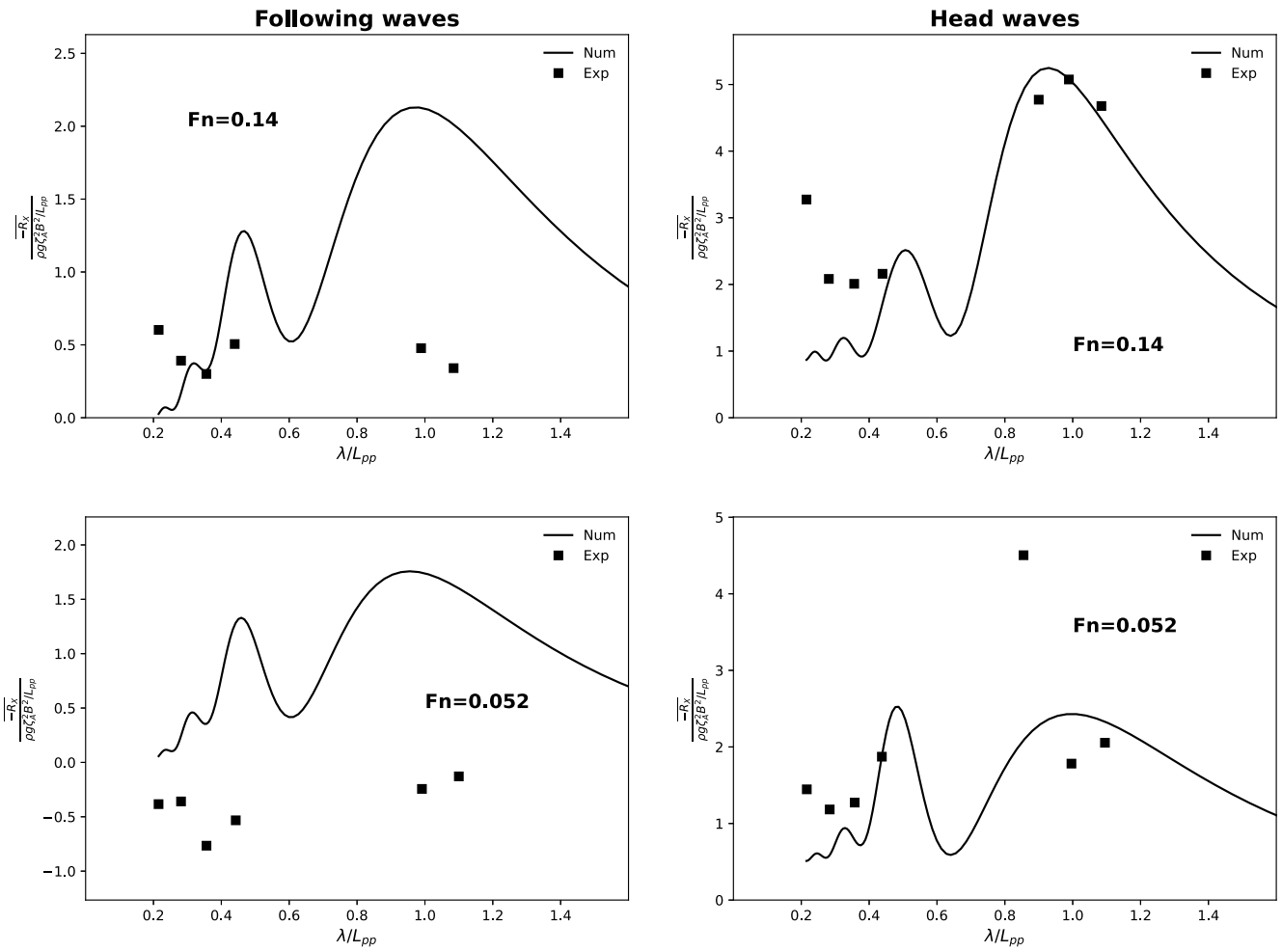

Fig. 2. Added resistance for the DTC hull with Froude numbers 0.14 (upper row) and 0.052 (lower row). Numerical results are compared with experimental results from Sprenger and Fathi (2015). Left: Following sea. Right: Head sea.

It is common practice to further simplify Eqs. (16) and (17), by assuming that the drag coefficient is constant along the hull, $C_D(x) = C_D$. The argument behind such simplification is that the cross-flow principle is a relatively crude method. Hence a constant drag coefficient can give a rough estimate (Sutulo and Soares, 2011). However, in such model, it is difficult to choose a drag coefficient that is representative for the whole hull based on theoretical calculations or physical reasoning, and it can be tempting to let the drag coefficient be a parameter which can be "tuned" to improve the results.

The transverse forces and moments from flow separation can be dominant in a maneuver, which alludes the importance of accurate calculations of these loads. The relative importance of the transverse viscous loads in a 35° turning circle in calm water is exemplified in Fig. 4. The DTC hull is used in the example, and the cross-flow principle, with $C_D(x)$ as explained in the following, is applied to calculate the transverse viscous loads. We notice that the transverse viscous force and moment have opposite sign compared with the other significant loads, which entails that the resulting loads are very sensitive to the accuracy of these terms.

2.5.2. Estimation of steady drag coefficients for ship sections

Faltinsen (1990) lists several parameters that influence the drag coefficient: *Free-surface effects, beam–draft ratio, bilge radius, effects of laminar or turbulent boundary layer flow, bilge keel effects, and three-dimensional effects.*

Based on these considerations Shen (2018) presented a practical method to calculate drag coefficients for ship sections. The principle is to divide the hull into parts with similar geometry, use drag coefficients for a similar shape, then correct for relevant effects. We follow the same approach, and the main steps are explained.

It is well known that the Reynolds number has a strong influence on the drag coefficient. Roughly, we can divide the Reynolds number range into two regimes, the *sub-critical* range and the *super-critical* range. In the sub-critical regime, flow separation takes place before transition to turbulence in the boundary layer flow occurs, while in the super-critical regime the boundary layer flow turns turbulent up-stream of the separation point. The drag coefficient can differ significantly for blunt bodies in the sub- and super-critical regimes, due to the fact that flow separation, in general, occurs further down-stream once the boundary layer flow has become turbulent. Experiments by Aarsnes (1984) confirm this for typical ship sections. Often, the flow regime in model scale is laminar while it is turbulent in full scale, this needs to be accounted for. In the present work, the numerical simulations are performed in model scale. However, due to the size of the model and that turbulence stimulation was present during the experiments, coefficients for turbulent flow are applied.

The free surface tends to reduce the drag coefficient. According to Faltinsen (1990) the free surface acts as an infinitely long splitter plate as a first approximation. Investigations by Shen (2018) shows that, for different geometric shapes, splitter plates reduce the drag coefficient with an average of 27.3% compared with the same geometry without splitter plate in infinite fluid. Consequently, the drag coefficients calculated with the procedure below are reduced with 27.3%.

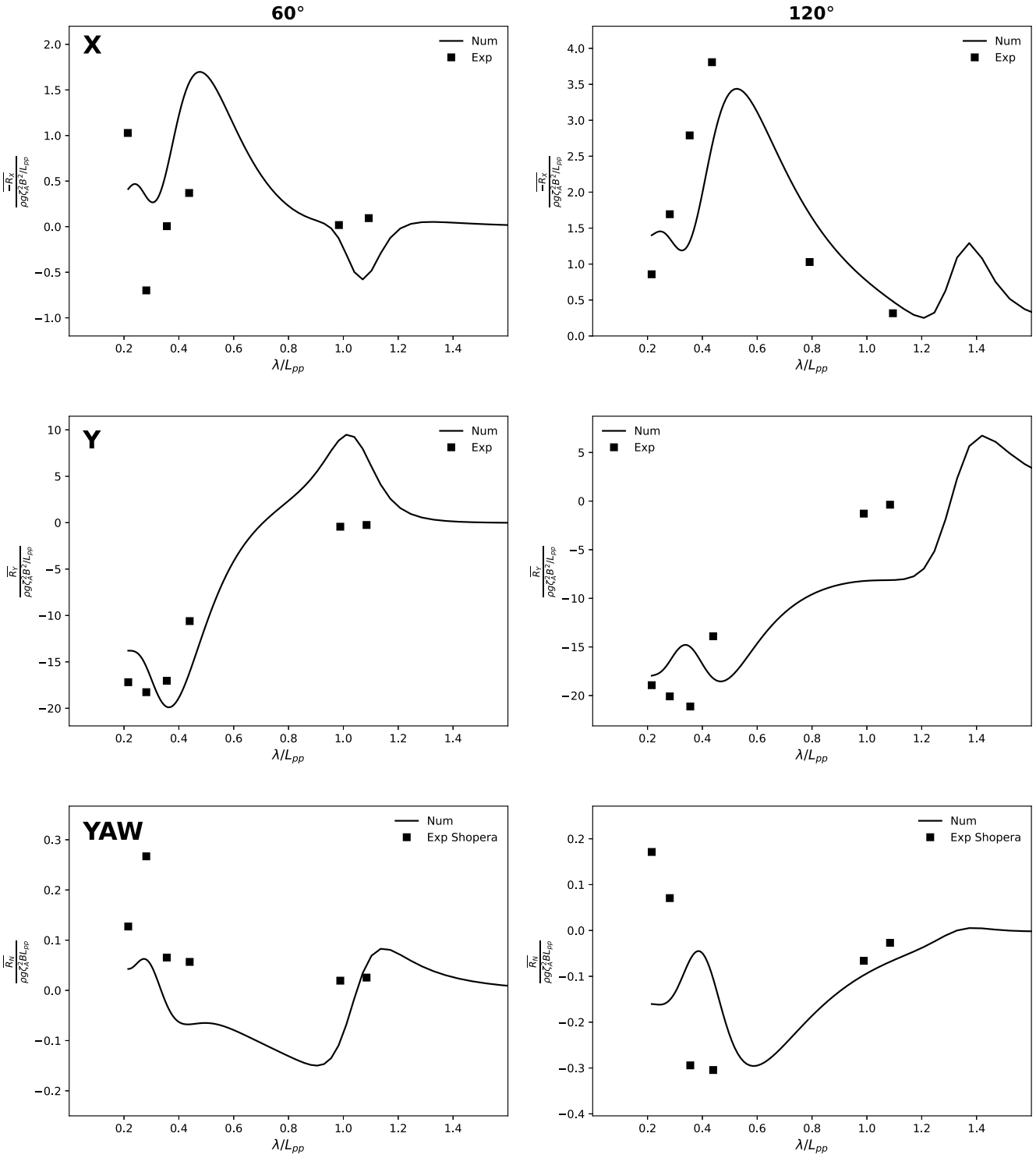

Fig. 3. Mean drift loads for the DTC hull in oblique waves, wave headings 60° (left) and 120° (right). Froude number 0.052. Numerical results are compared with experimental results from Sprenger and Fathi (2015). Upper: X-drift. Middle: Y-drift. Lower: Yaw-drift.

For maneuvers in waves, an error source is introduced by the fact that we do not have data for this factor in waves.

For the midship sections, which extends over most of the DTC hull, a rectangle with rounded corners can be a suitable simplification. Hoerner (1965) presents drag coefficients for both rectangular sections with sharp corners and rectangular sections with rounded corners. The former is a function of beam to draft ratio, while the latter is a function of bilge radius to draft ratio. The drag coefficients for rectangular sections with rounded corners are given for two cases: a square, and a rectangle with breadth to height ratio, $\frac{b}{2d} = 2.1$. Hence, to capture the effects of both beam to draft ration and bilge radius, we need to find a way to combine the drag coefficients for different beam to draft ratio and bilge radius.

Experiments by Tanaka (1983) indicate that the *bilge radius* has a strong effect on the drag coefficient. Faltinsen (1990) propose that the effect of bilge radius can be written as $C_D = C_1 e^{-kr_b/d} + C_2$. Here d is the draft, r_b is the bilge radius, Faltinsen (1990) suggests k may be 6. By using the drag coefficients from Hoerner (1965), both for

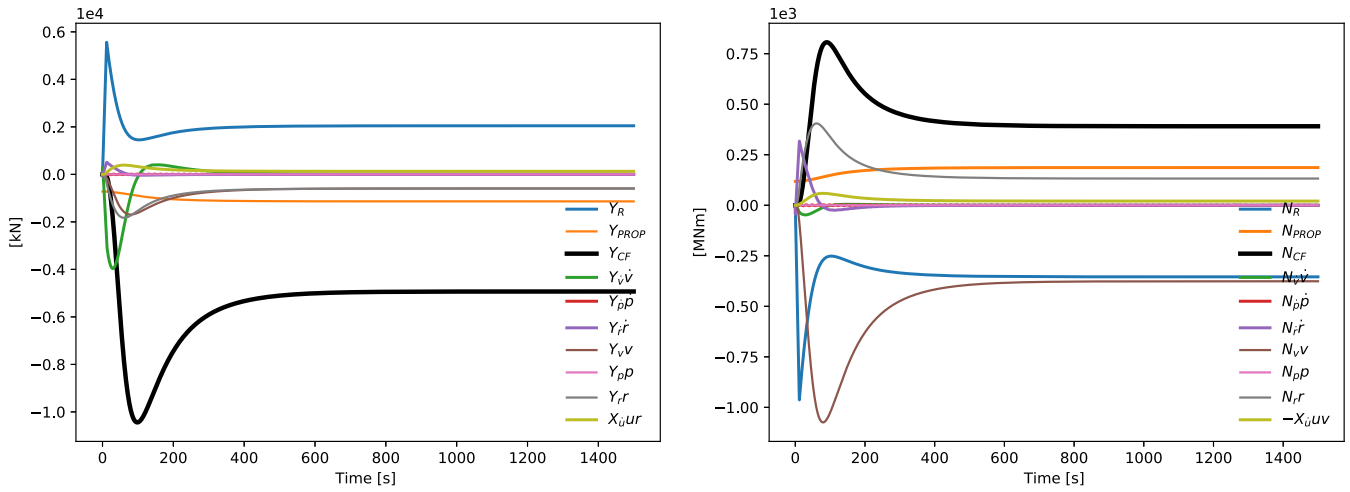

Fig. 4. External sway forces and yaw moments, for the DTC hull, during a Turning circle with 35° rudder angle in calm water, with initial Froude number 0.14. The transverse viscous loads are calculated according to the cross-flow principle and are represented by black color. Left: Sway forces, Right: Yaw moments. (For interpretation of the references to color in this figure legend, the reader is referred to the web version of this article.)

rectangles with sharp corners and rectangles with rounded corners, the constants C_1 and C_2 can be determined for each cross-section. Thus, we can obtain a drag coefficient that take into account both the beam to draft ratio and bilge radius.

The bilge keels will affect the midships drag coefficients. For oscillating roll motions, there are done extensive research on the effect of bilge keels, considering roll damping. For steady current the literature is less comprehensive. Experiments by Mercier and Huijs (2005) indicate that the drag coefficient, in steady flow, increases with at least 50% due to bilge keels. On the other hand, experiments by Faltinsen and Sortland (1987) show that the effect of bilge keel decrease with increasing Keulegan–Carpenter number $KC = \frac{U_m T}{d}$, where U_m is the amplitude of the oscillatory flow, T is the period of oscillation, and d is the characteristic size of the body, e.g the draft of a ship section. They tested a ship section without bilge keels and with bilge keels, for two different bilge keel dimensions. For small KC numbers the increase in drag coefficient due to bilge keels was up to 146%, while for KC = 13 the increase due to bilge keels was below 47%. Admittedly, their results are only for KC numbers up to 13, hence it is difficult to conclude for steady flow. Another important effect of the bilge keels is that the separation point will be fixed, which will reduce the scale effects due to turbulent or laminar boundary layer flow. In the present work, the effect of bilge keels is modeled by setting the bilge radius to zero, i.e. we use drag coefficients for rectangular sections with sharp corners, which will fix the separation point at the sharp corner. This can increase the drag coefficient significantly compared to a rectangle with rounded corners. To exemplify this, the drag coefficient for a rectangle with beam to draft ratio $\frac{b}{2d} = 2.1$ with sharp corners is 1.4, while with rounded corners the drag coefficient varies from 0.46 to 1.4 depending on the bilge radius (Hoerner, 1965).

The local inflow velocity at the ship ends is reduced due to three-dimensional effects, i.e. that flow separation from the ship ends create a back-flow opposing the incident flow, which will reduce the total drag force (Aarsnes, 1984; Faltinsen, 1990). In the present work, the reduction of drag coefficients due to three-dimensional effects are taken care of by using the reduction curve from Aarsnes (1984). This reduction curve, transferred to the DTC hull, is presented in Fig. 5.

The method is now exemplified for a section at x = 53.13 m. A selection of DTC hull sections is illustrated in Fig. 6, where this section is indicated with blue color. The breadth, draft, and bilge radius of this section are 51 m, 14.5 m, and 10.18 respectively. This section has not bilge keels, and the section is simplified as a rectangle with rounded corners. The breadth to height ratio, $\frac{b}{2d}$, is 1.76. The first step is to estimate the drag coefficient for a rectangle with sharp corners and

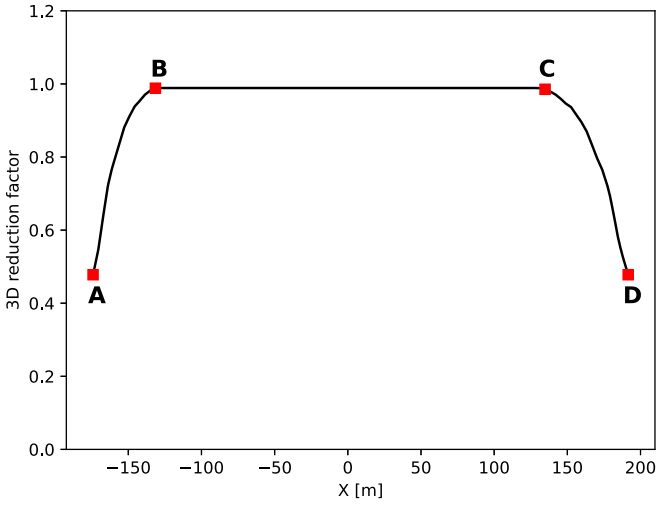

Fig. 5. 3D reduction factor along the DTC hull. The reduction is most significant at the ship end (A and D) where the reduction factor is 0.48. It increases rapidly, and between x = −131.5 and x = 134.8 (B and C) the reduction factor is 0.99.

breadth to height ratio $\frac{b}{2d} = 1.76$, from Hoerner (1965) we get $C_{D_{sharp}} = 1.62$. Next, the effect of rounded corners must be accounted for. In the expression $C_D = C_1 e^{-kr_b/d} + C_2$, $k = 6$ is used, while the constants C_1 and C_2 are estimated for the given cross-section. When the bilge radius goes towards infinity, $r_b \to \infty$, $C_D = C_2$. An estimate of C_2 is found by using the limiting value of C_D, when r_b has its maximum value. Hoerner (1965) presents drag coefficients as a function of bilge radius for a square cylinder and a rectangular cylinder with breadth to height ratio, $\frac{b}{2d} = 2.1$. The limiting value of C_D is interpolated between these two curves to get the value for breadth to height ratio $\frac{b}{2d} = 1.76$, we obtain $C_2 = 0.61$. When the bilge radius is zero, $r_b = 0$, $C_D = C_1 + C_2$, this corresponds to a rectangle with sharp corners. We can then write $C_1 = C_{D_{sharp}} - C_2 = 1.62\text{-}0.61 = 1.01$. The drag coefficient for a rectangle with breadth to height ratio $\frac{b}{2d} = 1.76$, corrected for rounded corners, can now be written as $C_{D_{round}} = 1.01e^{-6*10.18/14.5} + 0.61 = 0.63$. We observe that this value is close to C_2, which is the limiting value for large bilge radius. We consider free-surface effects by reducing the drag coefficient by 27.3%, $C_{D_{surf}} = 0.727 C_{D_{round}} = 0.46$. Finally, the drag coefficient is corrected for 3D effects by applying the correction factor

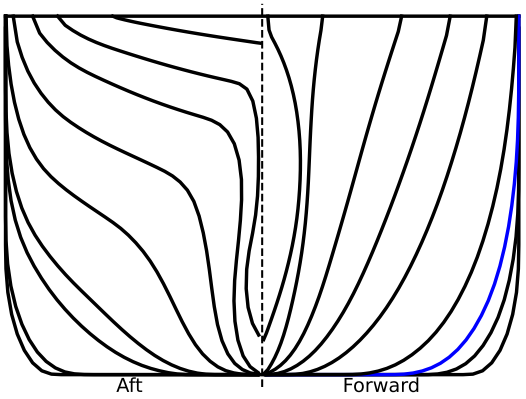

Fig. 6. A selection of DTC hull sections. The section at x = 53.13 m is indicated with blue. (For interpretation of the references to color in this figure legend, the reader is referred to the web version of this article.)

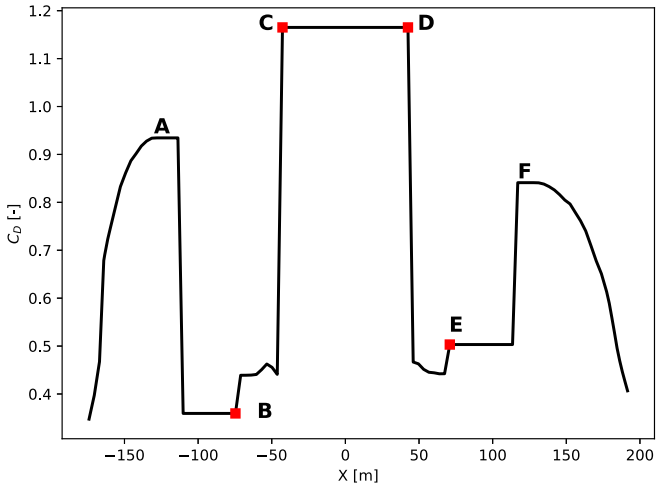

Fig. 7. Steady drag coefficients along the DTC hull. Between **B** and **E**, C_D is calculated according to the procedure in Section 2.5.2 with a rectangle as a base geometry. For the rest of the ship, drag coefficients are obtained from similar ship sections in Aarsnes (1984). At the ship ends, behind **A** and in front of **F**, C_D is reduced due to 3D-effects. Bilge keels are present between **C** and **D** which explains the sudden jump in C_D.

in Fig. 5. For this section the reduction factor is 0.99, and we obtain the final estimate $C_D = 0.99 C_{D_{surf}} = 0.45$.

The resulting steady drag coefficients for the DTC hull are presented in Fig. 7. Between **B** and **E**, the drag coefficients are calculated according to the procedure described above, with a rectangle as a base geometry. For the rest of the ship, drag coefficients are obtained from ship sections in Aarsnes (1984) that resemble the DTC hull section best. Since the calculations in Aarsnes (1984) were executed for 2D sections with a double body approximation, these sections are also corrected for free-surface effects and 3D-effects, as described above. Bilge keels are present between **C** and **D**, which explains the sudden jump in the drag coefficient. At the ship ends, **A** and **F**, drag coefficients for bow and stern sections from Aarsnes (1984) are applied. The reduction at the ship ends, behind **A** and in front of **F**, is due to 3D-effects.

The presented procedure is a pragmatic method to estimate drag coefficients. Of course, there are uncertainties in the simplifications, e.g the bilge keels are modeled in a very simplified way. Furthermore, at the ship ends, drag coefficients are chosen from similar geometries in Aarsnes (1984). It is possible to improve the method. However, the focus was to develop a pragmatic, easy to implement, method that is based on physical considerations. Moreover, in Shen (2018), the estimated drag coefficients for a tanker and well boat showed good agreement with experiments.

2.5.3. 2D+t theory

The cross-flow principle, as described in Section 2.5.1, assumes no interaction between the strips. Hence, it may, in reality, be justified only for large drift angles. This assumption can be valid for the steady time window of a tight turning circle. In the initial stage of a turning circle or for other maneuvers, e.g a zig-zag maneuver, this assumption is violated.

Faltinsen (2005) presented a 2D+t method for the transverse viscous loads, where the flow around each strip is developing in time. Eqs. (16) and (17) can still be used to calculate the sway force and yaw moment, but the drag coefficients $C_D(x)$ are updated every time step, i.e. the drag coefficient curve along the hull will look different for different drift angles. Faltinsen (2005) exemplified the method with a circular cylinder with forward speed and constant drift angle. A 2D+t coordinate-system is illustrated in Fig. 8. If we consider a vessel traveling through an Earth-fixed plane (Π), from this plane the problem transforms into a transient flow passing a 2D ship section, where the geometry changes with time. The sway force and yaw moment are then obtained from a series of 2D time-dependent flows around each cross-section. The physical reasoning behind this approach is that a vortex needs time to develop. Before a steady vortex pattern is obtained, the drag coefficient will vary in time. Analogous to a two-dimensional cross-section in a start-up flow, a vortex will initiate in the ship bow region and develop along the ship.

Alsos and Faltinsen (2018) generalized the method for a dropped circular cylinder, which was free to move in all six rigid-body degrees of motion with arbitrarily large angles. This is in principle a generalized maneuvering problem. Following Alsos and Faltinsen (2018) we want to express how the drag coefficient $C_D(x)$ varies along the ship within a certain time interval. This will depend on the previous ship motions. Assuming horizontal velocities and angular velocities to be constant, we can exemplify the procedure. We denote by t_0 the time instant that the bow is located at the $\Pi-$plane. We can then write

$$x_b - x_p = \int_{t_0}^{t} u dt = u(t - t_0) \tag{18}$$

where x_b is the $x-$coordinate of the bow, and x_p is the $x-$coordinate, in the body-fixed coordinate system, of the Earth-fixed $\Pi-$plane at any time instant. The distance the ship has moved transversely in the y-direction since the ship bow penetrated the Earth-fixed plane, can be expressed as:

$$s_y = \int_{t_0}^{t} [v(\tau) + x_p(\tau) r(\tau)] d\tau = v \frac{x_b - x_p}{u} + \frac{r}{u}[x_b(x_b - x_p) - \frac{1}{2}(x_b - x_p)^2] \tag{19}$$

We denote by $s = |s_y|$, and we can now express the non-dimensional displacement as

$$t' = \frac{s}{d} \tag{20}$$

where d is the sectional draft. This non-dimensional displacement is equivalent to the non-dimensional time, $t' = \frac{ut}{d}$, for a stationary flow (Faltinsen, 2005). Eq. (19) and (20) are used to express the non-dimensional time for a given cross-section at the time instant t. x_p is then the $x-$coordinate of the given cross-section, while u, v, and r are the surge velocity, sway velocity, and yaw-rate at the time instant t. This non-dimensional time t' is used to select the correct drag coefficient $C_D(t')$. To calculate the transverse viscous loads, $C_D(x)$ in Eqs. (16) and (17) is replaced with $C_D(t') = C_D(t'(x, u, v, r))$. In contrast to the cross-flow approach, where the sectional drag coefficient $C_D(x)$ is a function of x only, the sectional drag coefficient in a 2D+t approach is also dependent on the surge velocity, sway velocity, and yaw rate.

The challenge now is to express the time-varying drag coefficient $C_D(t')$ for every cross-section. When the non-dimensional time, t', is calculated for a cross-section, time varying drag coefficients $C_D(t')$ for a

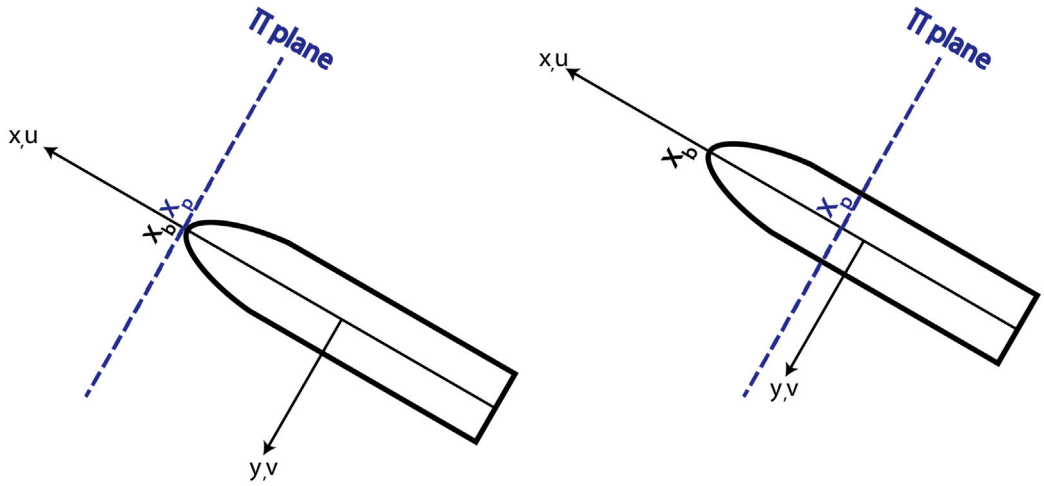

Fig. 8. 2D+t illustration. Left: Vessel reaches the Earth-fixed plane. Right: Vessel is passing through the Earth-fixed plane.

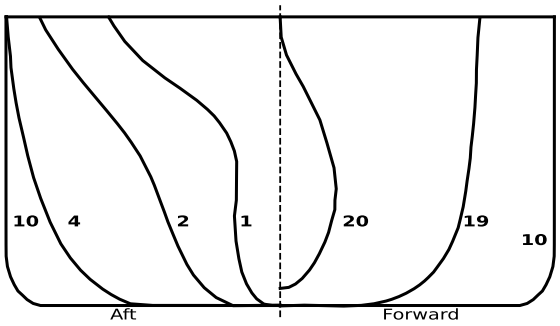

Fig. 9. Ship sections from Aarsnes (1984). The beam is 32.25 m and the draft is 12.40 m for this hull. Time-varying drag coefficients for these sections were calculated with a vortex sheet method by Aarsnes (1984), these coefficients are presented in Fig. 10.

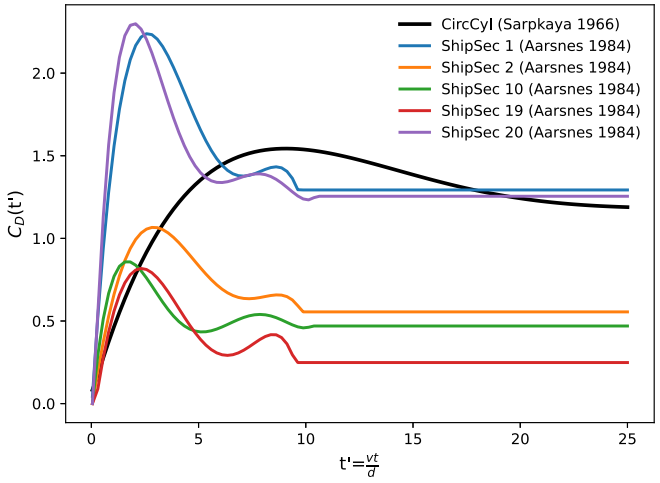

Fig. 10. Time-varying drag coefficients for ship sections in Aarsnes (1984) in a start-up flow. The geometry of these sections are presented in Fig. 9. Time-varying drag coefficients for a circular cylinder from Sarpkaya (1966) are indicated with a black line. (For interpretation of the references to color in this figure legend, the reader is referred to the web version of this article.)

2D cross-section in a startup flow, can be applied as the drag coefficient. For circular cylinders there exist numerical and experimental results for startup flows. However, for typical ship sections there are limited results for time-varying drag coefficients. Aarsnes (1984) published numerical results, calculated with a vortex sheet method, for some typical ship sections. The geometry of these sections are presented in Fig. 9, while the time-varying drag coefficients are presented in Fig. 10. Time-varying drag coefficients for a circular cylinder from Sarpkaya (1966) are included as a reference. For the circular cylinder, the radius R is taken as d. The drag coefficients for a circular cylinder and ship sections share similar qualitative behavior, increasing from a low value and having a peak before it reaches its steady value. However, the development for the ship sections has a quite distinctly shorter time scale than for the circular cylinder. The maximum value for the circular cylinder is for $t' = 9.09$, while the maximum value for the ship sections occurs for t' below 3 for all ship sections tested by Aarsnes (1984). This time scale is confirmed by Arslan et al. (2016), who performed CFD calculations of the same ship sections as in Aarsnes (1984). The time-varying drag coefficients are not presented in Arslan et al. (2016), they discussed development of flow patterns and vortices, these quantities were also discussed in Aarsnes (1984).

Table 1
Polynomial p_i-coefficients for Eq. (21).

p_1	p_2	p_3	p_4	p_5	p_6
$2.481 \cdot 10^{-7}$	$-3.647 \cdot 10^{-5}$	$1.906 \cdot 10^{-3}$	$-4.417 \cdot 10^{-2}$	$4.315 \cdot 10^{-1}$	$7.339 \cdot 10^{-2}$

It is believed that the different time scale is due to the shape of typical ship sections, where the separation point will vary less, and reach a steady position earlier than for a circular cylinder. However, more research is needed for the time-dependent drag on ship sections.

Alsos and Faltinsen (2018) used results from Sarpkaya (1966) as a basis for flows around a circular cylinder with different Reynolds numbers. Faltinsen (2005) constructed a polynomial based on the results from Sarpkaya (1966), Alsos and Faltinsen (2018) scaled this polynomial in the following way:

$$C_d(t') = (p_1 t'^5 + p_2 t'^4 + p_3 t'^3 + p_4 t'^2 + p_5 t' + p_6)\frac{C_{D,\infty}}{1.2} \tag{21}$$

where $C_{D,\infty}$ is the steady drag coefficient for a circular cylinder for a given Reynolds number and 1.2 is the steady drag coefficient for the Reynolds number in Sarpkaya (1966). Meaning that the profile is the same as in Sarpkaya (1966), but the steady value tends towards $C_{D,\infty}$. The coefficients p_1-p_6 are given in Table 1.

As a first naive approach, we implement a similar 2D+t method for ship sections. Time-varying drag coefficients are constructed by using steady drag coefficients for ship sections, $C_{D,\infty}$, calculated with the procedure in Section 2.5.2, combined with time-varying drag coefficients from similar ship sections in Aarsnes (1984).

For each ship section of the DTC hull a section that resembles this most closely is chosen from Fig. 9. The time-varying drag coefficient for

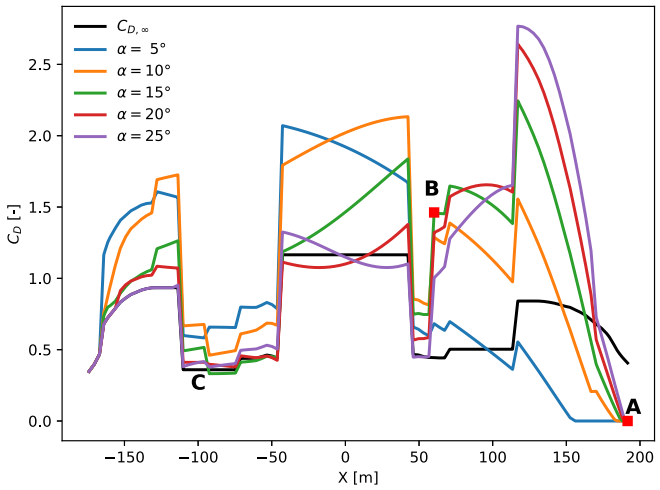

Fig. 11. C_D(t') along the DTC hull for different drift angles α. Using a naive interpretation of time-varying drag coefficients from Aarsnes (1984), referred to as $2D + t^0$. Constant yaw-rate, $r = 0.50$ deg/s. Steady C_D in pure cross-flow is illustrated with the black line. **A**: C_D starts at a low value and increases according to time-series in Fig. 10. **B**: A different time-series (hull shape from Aarsnes, 1984) is applied, which causes a sudden drop in C_D. **C**: From this point and backward, for $\alpha = 25°$, C_D is almost identical as the steady value. C_D for lower drift angles differ significantly from the steady value also in this region. (For interpretation of the references to color in this figure legend, the reader is referred to the web version of this article.)

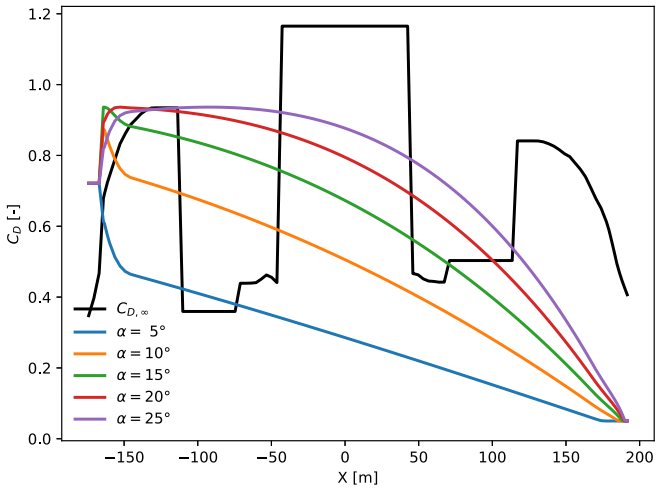

Fig. 12. C_D(t') along the DTC hull for different drift angles α. C_D(t') for a circular cylinder is scaled with the mean steady C_D along the hull. This method is referred to as $2D+t^{cyl}$. Constant yaw-rate, $r = 0.50$ deg/s. Steady C_D in pure cross-flow is illustrated with the black line. (For interpretation of the references to color in this figure legend, the reader is referred to the web version of this article.)

this section is then scaled with the steady drag coefficient $C_{D,\infty}$. This means that different time-histories are applied along the ship.

The cross-section at x = 53.13 m (Fig. 6) is used to exemplify the method. In Section 2.5.2 the steady drag coefficient, $C_{D,\infty}$, was estimated to 0.45. For this cross-section, section 10 in Fig. 9 is considered to be the most similar cross-section. The green curve in Fig. 10 is therefore considered. The simulations in Aarsnes (1984) ended at $t' \approx 9.5$, before reaching a steady value, judging from Fig. 10. We use the value at the end of the time-series as the steady value, which is 0.47 for the green curve. Meaning that the entire curve is multiplied by $\frac{C_{D,\infty}=0.45}{0.47} = 0.96$. The $C_D(t')$ value from this curve, which corresponds to t' calculated by Eqs. (19) and (20), is then used in the calculation of the transverse viscous loads.

An example of how the transient drag coefficient can vary along the DTC hull, using this method, for different drift angles is presented in Fig. 11. At the bow (**A**), the drag coefficients begin at a low value before they increase according to the given time-series in Fig. 10. At some sections along the hull, the drag coefficient is significantly higher than the steady value. This is due to the overshoot which can be observed in Fig. 10. At sections where the time-series applied is changed, i.e time-varying drag coefficient for a different ship section in Aarsnes (1984) is used, sudden jumps occur in the drag coefficient. This can be observed at **B**. There are also sudden jumps in C_D at positions where the steady coefficient varies considerably between different sectional forms. In a 2D+t approach, where we imagine a vortex developing along the hull, these sudden jumps are not physical and inconsistent with the assumption behind the method. In the rest of the paper, this naive implementation is referred to as $2D + t^0$.

A vortex develops continuously and cannot suddenly appear or disappear. To be consistent with the 2D+t assumption, we therefore in reality need to construct a $C_D(t')$-curve that develops continuously along the hull. A first attempt can be to use the time-variation for a circular cylinder, but use for $C_{D,\infty}$ the mean of the steady C_D along the hull. The steady C_D for the DTC hull is presented in Fig. 7 and the mean value is 0.73. Meaning that $C_D(t')$ is calculated by Eq. (21) with $C_{D,\infty} = 0.73$. The drag coefficient along the hull for different drift angles, following this approach, is presented in Fig. 12. In the rest of the paper this method is referred to as $2D+t^{cyl}$. The benefit of this method is that C_D varies continuously along the hull, which is more physical compared to the $2D+t^0$ method. However, the actual ship geometry is not represented. One consequence is that the time-variation is slower than one may expect.

In the following a third 2D+t method is presented. The time-derivative, $\frac{dC_D(t')}{dt'}$, can be estimated from the time-varying drag coefficients in Fig. 10. The curves that best resembles the DTC hull sections are chosen and scaled in the same manner as with the 2D+t^0 approach. Instead of using the drag coefficients directly, the time-derivative, $\frac{dC_D(t')}{dt'}$, is estimated based on the scaled time-varying drag coefficients and integrated along the hull. Again, the section at x = 53.13 m is used as an example. Similar as for the $2D + t^0$ method, the green curve in Fig. 10 is multiplied by $\frac{C_{D,\infty}=0.45}{0.47} = 0.96$. This curve is now used to estimate the time-derivative, $\frac{dC_D(t')}{dt'}$, at this cross-section for the given t'.

When the time-derivative is calculated for all ship sections and assuming that the drag coefficient is zero at the ship bow, a $C_D^*(t')$-curve can be obtained by integrating along the hull:

$$C_D^*(t') = C_D(t_0) + \int_{t_0}^{t'} \frac{C_D(t)}{dt} dt \tag{22}$$

From Eq. (22) a smooth curve is obtained, as in the $2D + t^{cyl}$ method, but at the same time takes into account the variation of the geometry along the hull. The next step is to scale the entire curve, such that when t' goes towards infinity, the calculated drag goes towards the steady drag, as in the cross-flow principle. If we imagine a drift angle close to 90°, t' will be very large along the entire hull, thus there is a steady cross-flow for all ship sections. In such situation, we want the 2D+t method to estimate similar transverse viscous loads as the cross-flow principle. Since the numerical results in Aarsnes (1984) ends at t' = 9.5, we assume the flow is steady at t' = 9.5. If t' at the stern is equal or greater than 9.5, we have a steady flow at the stern. We can then scale the curve from (22) with the mean value of the steady drag coefficient along the ship, $C_{D,\infty}$. However, If t' is lower than 9.5 at the stern, the flow has not reached a steady state along the hull. Then, we continue to integrate behind the ship until t' = 9.5. We assume that the flow is steady for this fictitious section some distance behind the hull. The time-varying drag coefficients along the hull can now be estimated as:

$$C_D(t') = \frac{C_{D,\infty}}{C_D^*(t' = t'_\infty)} C_D^*(t') \tag{23}$$

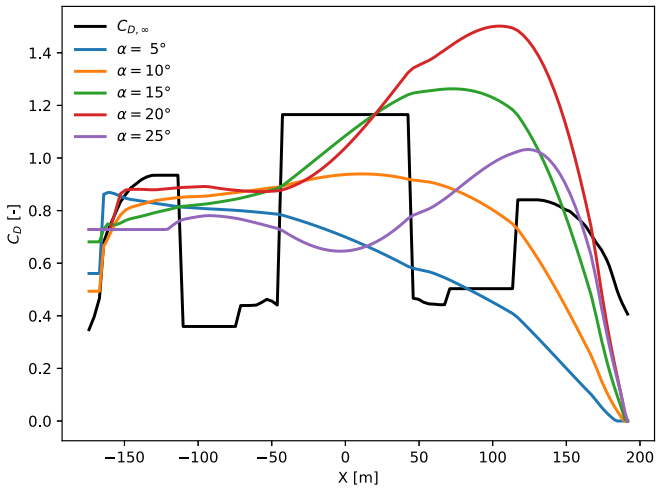

Fig. 13. C_D(t') along the DTC hull for different drift angles α. The curves are integrated based on $\frac{C_D(t')}{dt'}$ estimated from time-varying drag coefficients in Aarsnes (1984). This method is referred to as $2D+t$. Constant yaw-rate, $r = 0.50$ deg/s. Steady C_D in pure cross-flow is illustrated with the black line. (For interpretation of the references to color in this figure legend, the reader is referred to the web version of this article.)

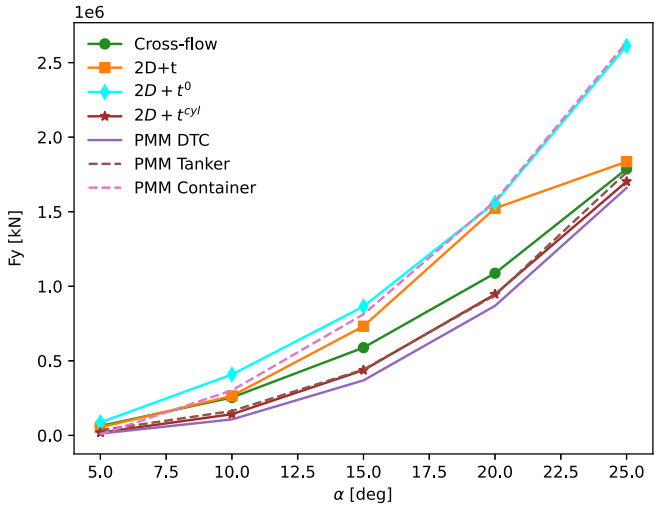

Fig. 14. Sway-force for a range of drift angles, α. Forward speed 16 knots (Fn = 0.14), yaw-rate r = 0.50 deg/s. Calculations by the present cross-flow approach, $2D+t^0$, $2D+t$, and $2D+t^{cyl}$ approaches. The results are compared with virtual PMM test of the DTC hull from Kinaci et al. (2019). PMM test from Brix (1993) for a tanker and a container ship are included for qualitative comparison. The first order hydrodynamic coefficients from the PMM tests are neglected.

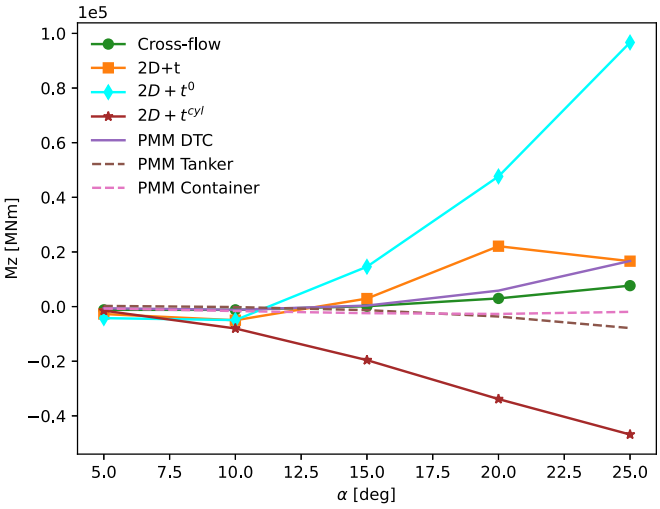

Fig. 15. Yaw moment for a range of drift angles, α. Forward speed 16 knots (Fn = 0.14), yaw-rate r = 0.50 deg/s. Calculated with the cross-flow approach, $2D + t^0$, $2D+t$, and $2D+t^{cyl}$. The results are compared with virtual PMM test of the DTC hull from Kinaci et al. (2019). PMM test from Brix (1993) for a tanker and a container ship are included for qualitative comparison. The first order hydrodynamic coefficients from the PMM tests are neglected.

where $C_{D,\infty}$ is the mean steady drag coefficient along the hull, $C_D^*(t')$ is the curve obtained from Eq. (22), and $C_D^*(t' = t'_\infty)$ is the value of $C_D^*(t')$ when t' goes towards infinity, for practical purposes this is when $C_D^*(t')$ reach a steady value. In Aarsnes (1984) the simulations ended at t' = 9.5, hence $t'_\infty = 9.5$. However, if you use other results, e.g. for other ship sections, the drag can go towards a steady value for a different t', t'_∞ is then chosen accordingly. $C_{D,\infty}$ in Eq. (23) is the same as the one used in the $2D + t^{cyl}$ method, for the DTC hull that will be the mean of the drag coefficients in Fig. 7, which is 0.73. This scaling ensures that the time-varying drag coefficients go towards the mean steady drag coefficient when t' goes towards infinity. However, for some drift angles this can be some distance behind the hull. For high drift angles, this 2D+t method will not predict the same transverse viscous loads as the cross-flow method presented in Section 2.5.1, it will predict the same transverse viscous loads as the simplified cross-flow approach, where a constant drag coefficient is applied along the hull. The drag coefficient along the hull for different drift angles, following this approach, is presented in Fig. 13. In the rest of the paper, this approach is referred to as $2D+t$. We note that there are significant differences between this method and the two other 2D+t methods (Figs. 11 and 12).

The sway force and yaw moment, on the DTC hull, for a range of drift angles, calculated with the cross-flow approach, $2D + t^0$, $2D + t$, and $2D + t^{cyl}$, are presented in Figs. 14 and 15. The forward speed is 16 knots, which corresponds to a Froude number Fn = 0.14, and the steady yaw-rate is 0.50 deg/s. The results are compared with Kinaci et al. (2019), they performed virtual PMM tests of the DTC hull and estimated the hydrodynamic coefficients. It is challenging to isolate different physical phenomena from PMM tests. Hence, the results from PMM tests includes non viscous contributions, while the presented cross-flow methods and 2D+t methods includes the transverse viscous loads from flow separation only. As a first approximation, the first order hydrodynamic coefficients are subtracted from the PMM tests for comparison reasons. Kinaci et al. (2019) performed virtual PMM test for drift angles up to 12° only. Hence, the results based on these PMM tests, presented in Figs. 14–15, for drift angles above 12° are associated with a significant uncertainty. As a qualitative comparison, hydrodynamic coefficients for a tanker and a container ship, presented in Brix (1993), are included.

For the conditions in Fig. 14, the sway-force calculated with $2D+t^{cyl}$ is close to the sway force from Kinaci et al. (2019), while the sway-force calculated with cross-flow, $2D + t^0$ and $2D + t$ deviate slightly more. Especially the $2D + t^0$ method deviates from the other methods for drift angle 25°. However, as mentioned before, the PMM tests of the DTC hull were performed for drift angles up to 12°, and the results above 12° should be considered with care. Even if the sway force for a tanker and container ship from Brix (1993) are calculated for different hull shapes, the sway force is similar. For the yaw moment in Fig. 15, the different methods deviate significantly for drift angles above 10°. Especially the yaw moment calculated with $2D+t^{cyl}$ and $2D+t^0$stands out for high drift angles. This will probably affect the maneuvering behavior of the ship. One explanation for $2D + t^{cyl}$, can be that the flow separation, in particular at the vessel's bow, is not represented correctly when the geometry is simplified to a circular cylinder with varying radius. This observation was done in Ommani and Faltinsen (2014), where CFD calculations of a ship hull were compared with a

Table 2
Overview of presented methods to calculate transverse viscous loads.

Method	Cross-flow	$2D+t^0$	$2D+t^{cyl}$	$2D+t$
Base Geometry	DTC	DTC	Circular cylinder	DTC
Forward speed	No	Yes	Yes	Yes
Time-varying drag	–	From literature	From literature	Integrated, derivatives from literature
Consistent with assumptions	Questionable	No	Yes	Yes

circular cylinder with varying radius equal to the cross-sectional draft. For $2D+t^0$, we can see from Fig. 11 that the drag coefficient is very high around x = 120–150 m for high drift angles, which explains the behavior of the yaw moment.

The three methods presented, based on the 2D+t approach, are simplified methods based on time-varying drag coefficients from the literature. The only time-varying drag coefficients that were found for ship sections in the literature, were the results in Aarsnes (1984). This is an uncertainty of the method. Extending the 2D+t method with a 2D Navier–Stokes solver with an adaptive grid will increase the accuracy. However, this will make the method considerably more elaborate. To further develop the 2D+t method in a pragmatic manner, more research is needed for the time-varying drag coefficients for typical ship sections. However, like the cross-flow principle, the 2D+t approach is a simplified method that models a very complicated phenomena. The similarities and differences of the methods are summarized in Table 2.

2.5.4. Transverse viscous loads in waves

Drag forces in oscillatory flow have been given some attention in the literature. In addition to the parameters discussed in Section 2.5.2, the drag coefficient will also depend on the Keulegan–Carpenter (KC) number and the relative current $\frac{U_c}{U_m}$. where $U_m\cos(\omega t)$ is the oscillating part and U_c is the steady part of the relative flow. For combined oscillatory flow and current, the research is more limited. Experiments by Sarpkaya and Storm (1985) and Hamel-Derouich (1993) show that the drag coefficient in waves alone, in general, overestimates the drag coefficient in combined waves and current. In fact, results in Hamel-Derouich (1993), for $U_c/U_m > 1$, show that the drag coefficient in combined waves and current is close to the coefficient in current only. Shen et al. (2019) explains this with, for $U_c/U_m > 1$, the returning vorticity due to the oscillatory part has a small influence on the inflow velocity to the body. In the present work, a preliminary attempt to account for the combined wave and current was made, using existing data for the KC-dependent C_D of simplified geometries (but with $U_c = 0$). However, the transverse viscous loads were unreasonably large. We follow Shen et al. (2019) and neglect the effect of waves in the calculation of the transverse viscous loads. The interaction of oscillatory and steady flow is a subject which needs further research.

3. Experimental setup

The numerical simulations are compared with free-running maneuvering tests performed in the Ocean basin at SINTEF Ocean in Trondheim. Details of the test program and experimental setup are described in Rabliås and Kristiansen (2019). Course keeping tests, turning circles, and Zig-Zag tests were performed in calm water conditions and in regular waves. Seven wavelengths, in the range $\lambda/L_{pps} = 0.280$–1.120 were tested. A 63.65 scale of the Duisburg Test Case (DTC) was used in the experiments. The model was made at SINTEF Ocean in conjunction with the SHOPERA project (Sprenger and Fathi, 2015). Detailed information about the hull, propeller, and rudder can be found in el Moctar et al. (2012). The main particulars of the model are presented in Table 3.

Table 3
Ship particulars.

Particulars		Ship	Model
L_{pp}	[m]	355	5,577
B	[m]	51	0,801
d	[m]	14,5	0,228
Δ	[kg]	173468000	672,6[a]
C_B	[–]	0,661	0,661
x_G[b]	[m]	174,059	2,721[a]
y_G	[m]	0	0
KG	[m]	19,851	0,314[a]
GM	[m]	5,100	0,078[a]
I_{44}	[kgm^2]	7,148E+10	45,43[c]
I_{55}	[kgm^2]	1,322E+12	1266,330[a]
I_{66}	[kgm^2]	1,325E+12	1268,4
L_{bk}	[m]	14,85	0,23[a]

[a]Measured values.
[b]Relative to aft perpendicular.
[c]Estimated from measured natural roll period and numerical added mass.

Table 4
Simulation parameters.

Parameter	Value
C_{TN}	0.5
Y_{PT}	−0.2278
k_m	0.55
thrust deduction, t	0.1070
wake fraction, w	0.24

4. Results

In the following sections, numerical simulations with the DTC hull are compared with experimental results from Rabliås and Kristiansen (2019). In the experiments it was observed an asymmetry in the rudder commands towards starboard and port side. This asymmetry was also observed during the SHOPERA project where the same model was tested. They suspect that the difference was caused due to that the rudder was mounted 3° off the true zero value (Shigunov et al., 2018). In the experiments presented in Rabliås and Kristiansen (2019) the zero rudder angle was controlled both before and after the tests. However, the difference in the starboard/port behavior was still observed. In the simulations in the current work, this is taken care of by introducing a lateral propeller force Y_{PROP} and yaw moment N_{PROP}. The lateral propeller loads are calculated according to Eq. (5).

No tuning is applied, meaning that the input parameters are the same for all simulations. Only the environmental conditions, initial velocity, and the calculation of the transverse viscous loads are changed between the different simulations. Values for C_{TN}, Y_{PT}, k_m, thrust deduction, and wake fraction can be found in Table 4. It is expected that the overall results could be improved if we chose to tune these parameters. However, the main objective of this work is to compare different methods of estimating the transverse viscous loads. The initial velocity in the experiments (measured values) and the numerical simulations are identical. At the beginning of a simulation, the propeller RPS is calculated to achieve this velocity, and this RPS is kept constant during the simulation, as in the experiments. All simulations are done in model scale. The presented results are scaled up to full scale by Froude scaling.

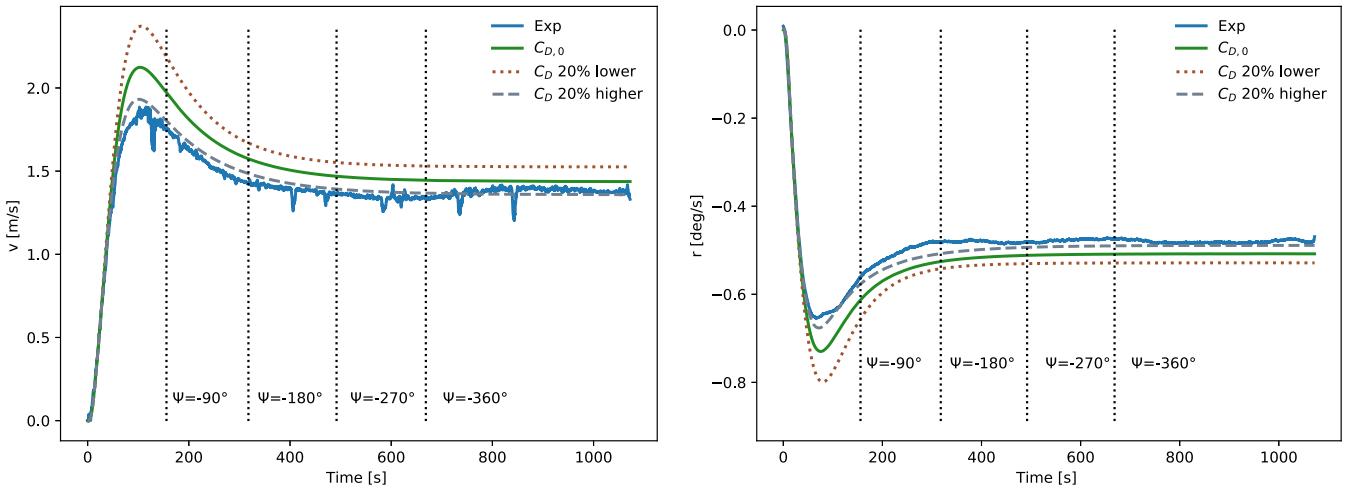

Fig. 16. Experimental and numerical results of a turning circle of the DTC hull with 35° rudder angle in calm water, with 16 kn approach speed (Fn = 0.14). The transverse viscous loads are calculated according to the cross-flow principle. Sensitivity of the drag coefficients are also presented. Left: Sway velocity. Right: Yaw-rate.

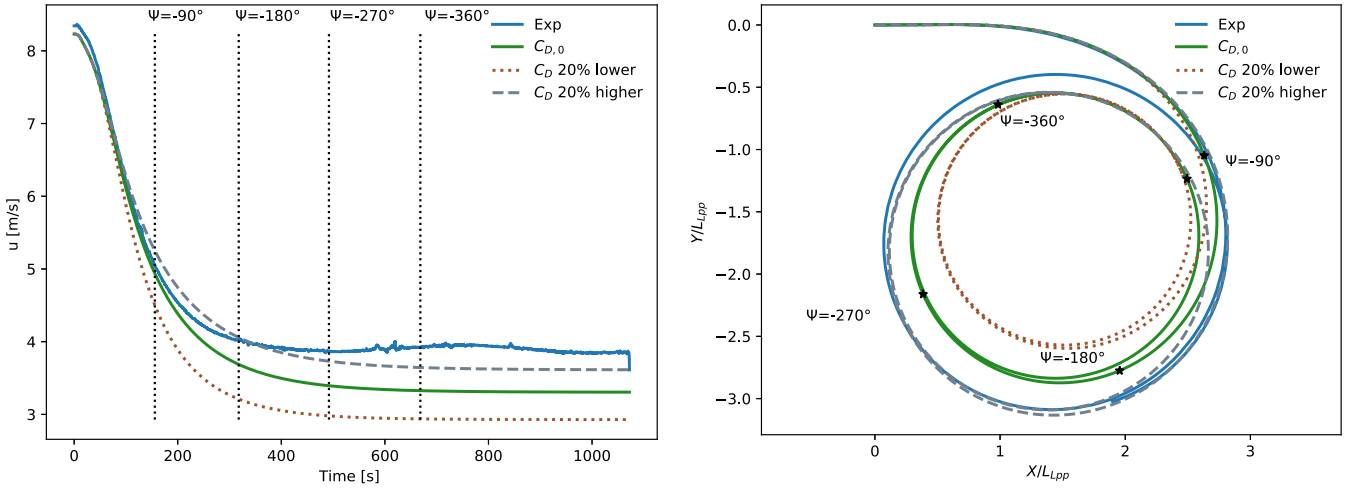

Fig. 17. Experimental and numerical results of a turning circle of the DTC hull with 35° rudder angle in calm water, with 16 kn approach speed (Fn = 0.14). The transverse viscous loads are calculated according to the cross-flow principle. Sensitivity of the drag coefficients are also presented. Time instants, from the simulation where $C_{D,0}$ is used, for heading $\Psi = -90°$, $-180°$, $-270°$, and $-360°$ are indicated. Left: Surge velocity. Right: Trajectory.

4.1. Cross-flow approach

A turning circle with 35° rudder angle towards starboard in calm water with approach velocity 16 kn, full scale, is considered. This corresponds to a Froude number Fn = 0.14. The cross-flow principle is used for the transverse viscous loads. To investigate the sensitivity to C_D, simulations are also performed with the drag coefficients increased and decreased by 20%. The results are shown in Figs. 16 and 17.

As we can see in Fig. 16, increasing the drag coefficients tends to reduce the sway velocity and the absolute value of the yaw-rate, in particular the peak values. By peak values we refer to the maximum which occurs in this case at 120 s. The surge velocity, presented in Fig. 17, is increased by increasing C_D due to coupling effects. For example gives the term $-C_{TN}Y_{\dot{v}}rv$ a significant contribution in the surge equation of motion (Eq. (1)). The inertia term $-Mrv$ is another coupling term, which affects the forward speed. These effects increase the steady diameter, which is demonstrated in Fig. 17. The opposite effects are observed when the drag coefficients are decreased. The results show that a 20% change of the drag coefficients has a significant effect on the trajectory, which emphasizes the importance of the transverse viscous loads. In fact, in simulations where the transverse viscous loads are neglected ($C_D = 0$), the results for the turning circle with 35° rudder angle becomes unphysically. For the results in Figs. 16 and 17, a 20% increase of C_D, i.e. $1.2C_{D,0}$, provides the best results overall. However, for the rest of the paper $C_{D,0}$, which are estimated according to the procedure in Section 2.5.2, are used as a reference for steady C_D.

4.2. 2D+t

In Figs. 18–21, results of the DTC hull, from turning circles with 35° rudder angle towards starboard in calm water with approach velocity 16 kn are presented. The transverse viscous loads are calculated with the three methods, based on the 2D+t approach, presented in Section 2.5.3, $2D + t^0$, $2D + t$, and $2D + t^{cyl}$. The results are compared with experimental results and with simulations where the cross-flow principle is applied.

In the trajectory in Fig. 18, we can see that the $2D + t$ method and $2D + t^{cyl}$ method has a good match with the experimental results. For the simulations where the cross-flow principle is applied, the trajectory follows the experiments in the initial phase, while the steady diameter is smaller than the experiments. The 2D+t^0 method, using scaled $C_D(t')$-curves from the literature directly, deviates from the experiments at an earlier stage compared to the other two methods and the steady circle is underestimated.

For the surge velocity in Fig. 19 we can see that the near steady speed reached towards the end of the test/simulation is best predicted

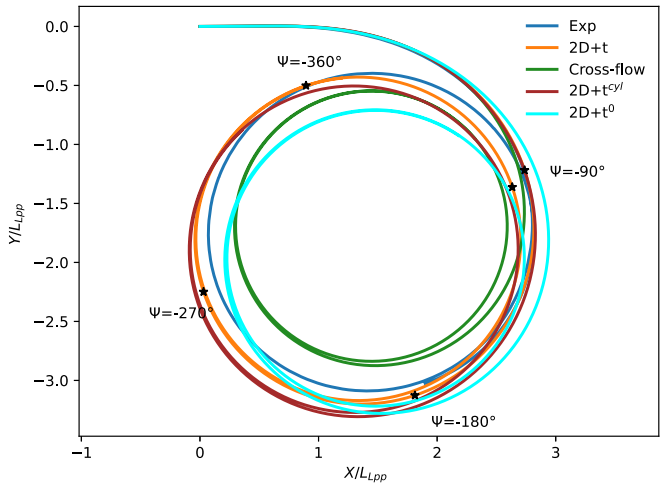

Fig. 18. Trajectory of a turning circle of the DTC hull with 35° rudder angle in calm water, with 16 kn approach speed (Fn = 0.14). Simulations where transverse viscous loads are calculated with pure cross-flow, $2D+t$, $2D+t^0$, and $2D+t^{cyl}$ are presented. Time instants, from the simulation with $2D+t$, for heading $\Psi = -90°$, $-180°$, $-270°$, and $-360°$ are indicated.

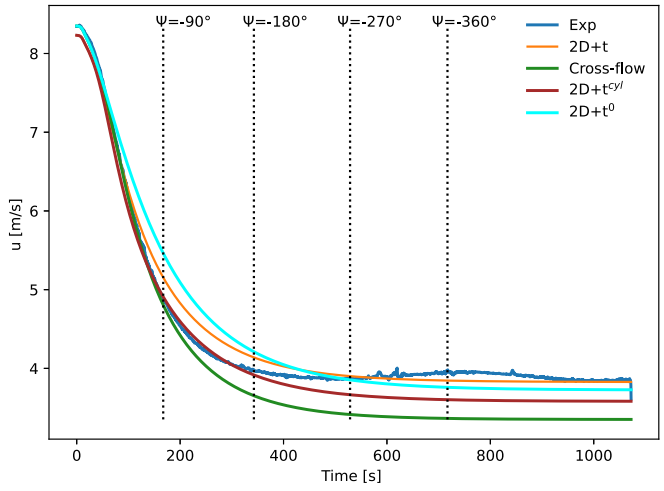

Fig. 19. Surge velocity of a turning circle of the DTC hull with 35° rudder angle in calm water, with 16 kn approach speed (Fn = 0.14). Simulations where transverse viscous loads are calculated with pure cross-flow, $2D+t$, $2D+t^0$, and $2D+t^{cyl}$ are presented. Time instants, from the simulation with $2D+t$, for heading $\Psi = -90°$, $-180°$, $-270°$, and $-360°$ are indicated.

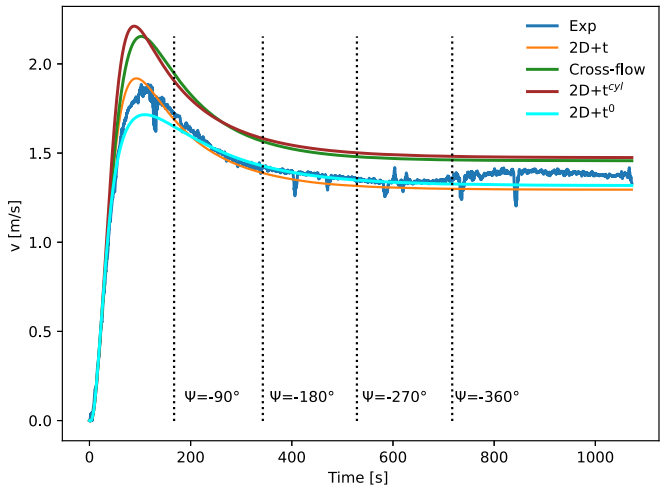

Fig. 20. Sway velocity of a turning circle of the DTC hull with 35° rudder angle in calm water, with 16 kn approach speed (Fn = 0.14). Simulations where transverse viscous loads are calculated with pure cross-flow, $2D+t$, $2D+t^0$, and $2D+t^{cyl}$ are presented. Time instants, from the simulation with $2D+t$, for heading $\Psi = -90°$, $-180°$, $-270°$, and $-360°$ are indicated.

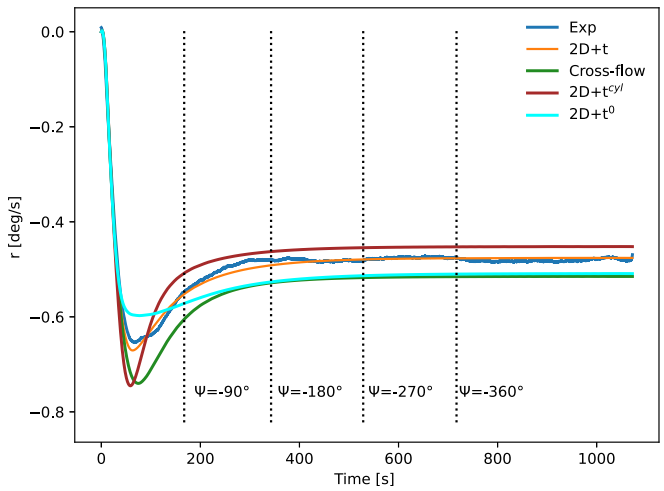

Fig. 21. Yaw-rate of a turning circle with 35° rudder angle in calm water, with 16 kn approach speed (Fn = 0.14). Simulations where transverse viscous loads are calculated with pure cross-flow, $2D+t$, $2D+t^0$, and $2D+t^{cyl}$ are presented. Time instants, from the simulation with $2D+t$, for heading $\Psi = -90°$, $-180°$, $-270°$, and $-360°$ are indicated.

by the $2D+t$ method and the $2D+t^0$ method. The $2D+t$ method and the $2D+t^{cyl}$ method predicts the initial deacceleration slightly better than the 2D+t^0 method This is consistent with the observations that were made in relation to the trajectory in Fig. 18.

The sway velocity, presented in Fig. 20, is significantly better represented with the $2D+t$ method and the $2D+t^0$ method compared to the other two methods.

The yaw-rate, presented in Fig. 21, shows that the $2D+t$ method, using time-integrated $C_D(t')$-curves, has a very good match with the experiments. The 2D+t^0 method and the cross-flow method predicts almost identical steady yaw-rate at the end of the maneuver. However, the cross-flow method under-predicts the minimum value, while the 2D+t^0 method over-predicts this value.

The initial stage of a turning circle is important in order to obtain accurate results from simulations. The error in this stage will accumulate during the maneuver. If we take a closer look at the yaw-rate in Fig. 21, the 2D+t^0 method over-predicts the negative peak, close to $t = 100$ s, while the near steady yaw-rate at the end of the simulation is better represented. This can be explained from Fig. 11, where we can observe that, for low drift angles, a sudden jump in the drag coefficient between $x = -100$ m and $x = -150$ m, which will increase the righting yaw moment. Due to coupling terms, this error will also affect the surge- and sway velocity. This emphasizes the importance of predicting the transverse viscous loads well for all drift angles, even for a steady maneuver as a turning circle.

4.3. Regular waves

A turning circle with 35° rudder angle towards starboard in regular waves with wavelength $\lambda/L_{pp} = 0.86$, wave steepness $H/\lambda = 1/40$, and head sea ($\beta_0 = 180°$) approach angle is considered. The initial velocity is 11.23 knots, which corresponds to Fn = 0.1. The results are presented in Figs. 22–28. Simulations where the transverse viscous loads are calculated with pure cross-flow, $2D+t$, and $2D+t^{cyl}$ are presented. Since the results in Section 4.2 with the 2D+t methods, using $C_D(t')$ for a circular cylinder and time-integrated $C_D(t')$ curves, turned

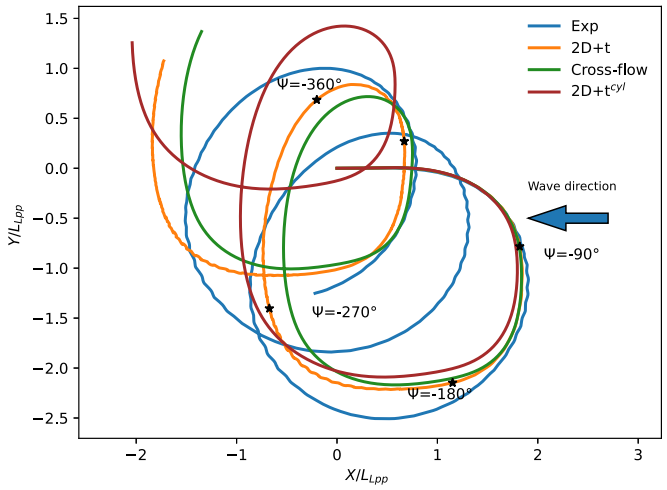

Fig. 22. Trajectory of a turning circle of the DTC hull with 35° rudder angle in regular waves with wavelength $\lambda/L_{pp} = 0.86$, wave steepness $H/\lambda = 1/40$, head sea ($\beta_0 = 180°$) approach angle, and 11.23 knots approach speed (Fn = 0.1). Simulations where the transverse viscous loads are calculated with pure cross-flow, $2D+t$, and $2D+t^{cyl}$ are presented. Wave direction is indicated with an arrow. Time instants, from the simulation with $2D+t$, for heading $\Psi = -90°$, $-180°$, $-270°$, and $-360°$ are indicated.

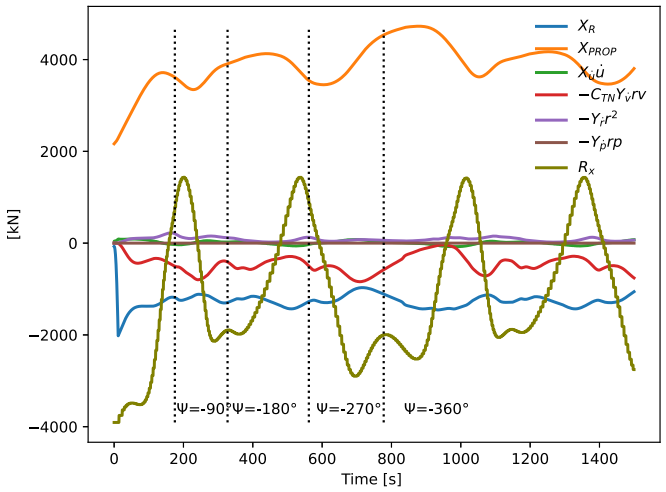

Fig. 23. External surge forces, from a simulation using the $2D+t$ method, during a turning circle with 35° rudder angle towards starboard, in regular waves with wavelength $\lambda/L_{pp} = 0.86$, wave steepness $H/\lambda = 1/40$, and initial head sea. The approach speed is 11.23 knots (Fn = 0.1). Time instants for heading $\Psi = -90°$, $-180°$, $-270°$, and $-360°$ are indicated.

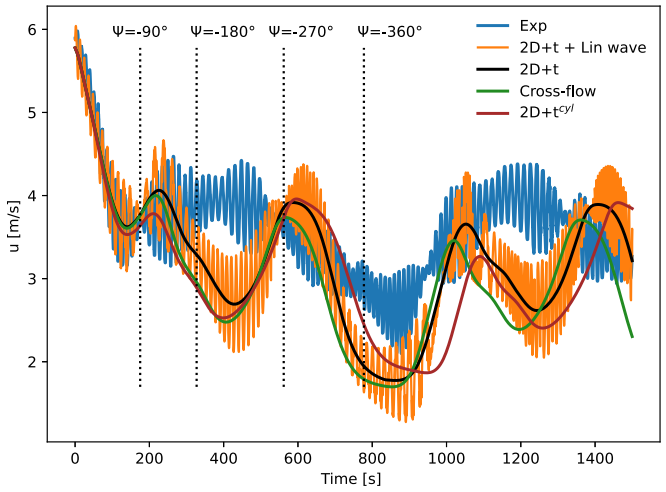

Fig. 24. Surge velocity of a turning circle of the DTC hull with 35° rudder angle in regular waves with wavelength $\lambda/L_{pp} = 0.86$, wave steepness $H/\lambda = 1/40$, head sea ($\beta_0 = 180°$) approach angle, and 11.23 knots approach speed (Fn = 0.1). Simulations where the transverse viscous loads are calculated with pure cross-flow, $2D+t$, and $2D+t^{cyl}$ are presented. Time instants, from the simulation with $2D+t$, for heading $\Psi = -90°$, $-180°$, $-270°$, and $-360°$ are indicated.

out to be more promising compared to the 2D+t^0 method, results with the 2D+t^0 method are omitted in the rest of the paper. Furthermore, these 2D+t methods are more consistent with the 2D+t assumption.

As we can see in Fig. 22, the numerical simulations follow the experimental trajectory closely in the initial phase of the turning. Overall, the $2D+t$ method has a better match with the experiments than the cross-flow approach, while the $2D+t^{cyl}$ method deviates slightly more than the other two methods. This is probably due to the deviating yaw moment at high drift angles for this method (cf. Fig. 15). During a simulation in regular waves, the drift angle will oscillate with a slowly-varying time-scale due to the change in wave heading, and the drift angle can be significantly higher than during a calm water simulation, which will amplify this effect. At heading $\Psi = -90°$, which corresponds to beam waves, the simulations start to deviate from the experimental results, for all the simulation models. Moreover, the second circle is tighter in the simulations compared to the experiments. Both the experimental results and the numerical results have a drifting path due to second order mean loads, but the numerical simulations seems to over-estimate the drifting angle.

The deviation from the experimental results is believed to be partly explained by the fact that the second order drift loads are not represented adequately for all wave headings, especially for following waves (Figs. 2 and 3). The external surge forces during the maneuver are presented in Fig. 23. For heading $\Psi = -180°$, the calculated added resistance, R_x, is relatively large. This can be recognized in Fig. 24, where we can see that the experimental results show a slight increase in the surge velocity for heading $\Psi = -180°$, while the surge velocity in the simulations continues to decrease for this heading. This indicates that the added resistance is over-predicted in the simulations. This is in accordance with the observations in Section 2.4, that the added resistance is over-predicted in following waves (Fig. 2). Calculating second order drift loads in following and oblique sea is a challenge. For following sea, the added resistance is often relatively small, and the sign can change with forward speed and wavelength.

In Figs. 24–26, linear wave-induced velocities are super-imposed to the surge velocity, sway velocity and yaw-rate. These velocities are added for illustration purposes and are not explicitly included in the maneuvering simulations. However, accurate representation of the linear wave motions are important when calculating the second order drift loads. Hence, such representation can be useful to check that the linear wave motions are satisfactorily represented. We can see that the amplitude of the linear wave-induced velocities are reasonable in comparison to the experimental values. Moreover, the low-frequency variability of the linear wave-induced velocities, for sway velocity (Fig. 25) and yaw-rate (Fig. 26), are similar to the experiments. This slowly varying behavior is due to the change in wave heading. For near beam sea conditions, the wave-induced sway velocity has a high amplitude, while the amplitude is small in near head sea and following sea. This is particularly true for the numerical simulations, where memory effects are neglected in the seakeeping calculations. The linear wave-induced yaw moment is relatively small for near beam sea conditions, hence the maximum yaw moment occurs for oblique sea.

The external sway forces and yaw moments during the maneuver are presented in Figs. 27 and 28. As we observed for calm water in Fig. 4, the contribution from the transverse viscous loads are of significant importance. Another dominant contribution comes from the second order drift force and drift moment due to regular waves. The

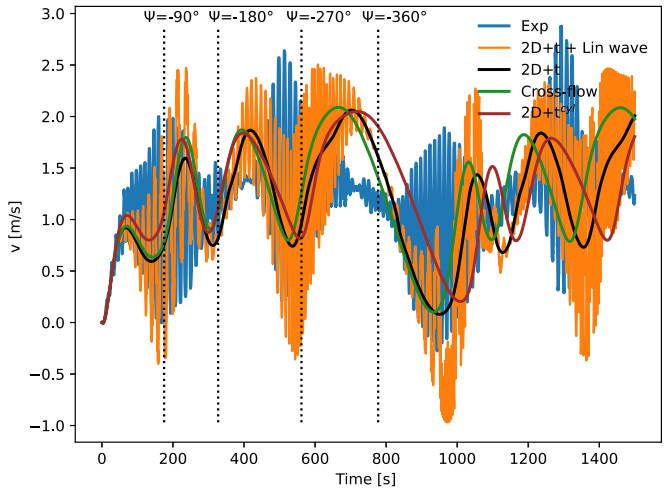

Fig. 25. Sway velocity of a turning circle of the DTC hull with 35° rudder angle in regular waves with wavelength $\lambda/L_{pp} = 0.86$, wave steepness $H/\lambda = 1/40$, head sea ($\beta_0 = 180°$) approach angle, and 11.23 knots approach speed (Fn = 0.1). Simulations where the transverse viscous loads are calculated with pure cross-flow, $2D + t$, and $2D + t^{cyl}$ are presented. Time instants, from the simulation with $2D + t$, for heading $\Psi = -90°$, $-180°$, $-270°$, and $-360°$ are indicated.

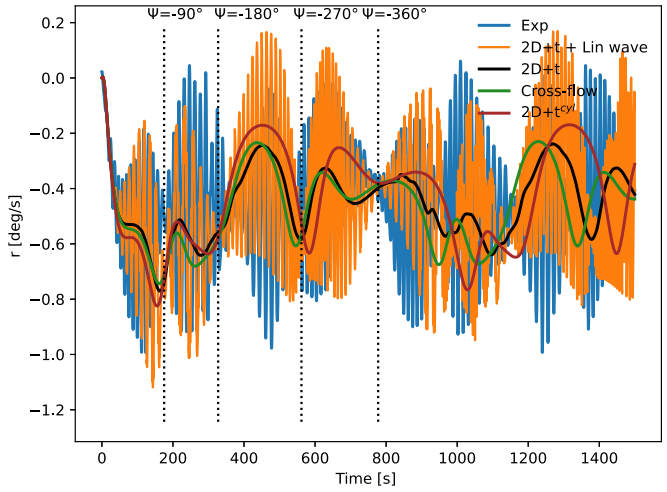

Fig. 26. Yaw-rate of a turning circle of the DTC hull with 35° rudder angle in regular waves with wavelength $\lambda/L_{pp} = 0.86$, wave steepness $H/\lambda = 1/40$, head sea ($\beta_0 = 180°$) approach angle, and 11.23 knots approach speed (Fn = 0.1). Simulations where the transverse viscous loads are calculated with pure cross-flow, $2D + t$, and $2D + t^{cyl}$ are presented. Time instants, from the simulation with $2D+t$, for heading $\Psi = -90°$, $-180°$, $-270°$, and $-360°$ are indicated.

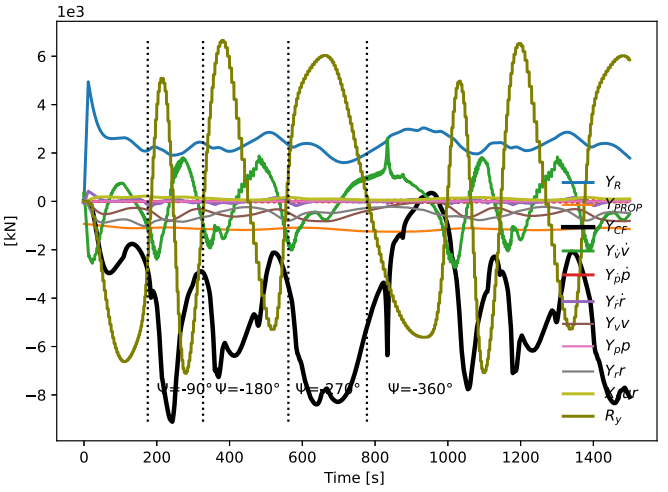

Fig. 27. External sway forces, from a simulation using the $2D + t$ method, during a turning circle with 35° rudder angle towards starboard, in regular waves with wavelength $\lambda/L_{pp} = 0.86$, wave steepness $H/\lambda = 1/40$, and initial head sea. The approach speed is 11.23 knots (Fn = 0.1). Time instants for heading $\Psi = -90°$, $-180°$, $-270°$, and $-360°$ are indicated.

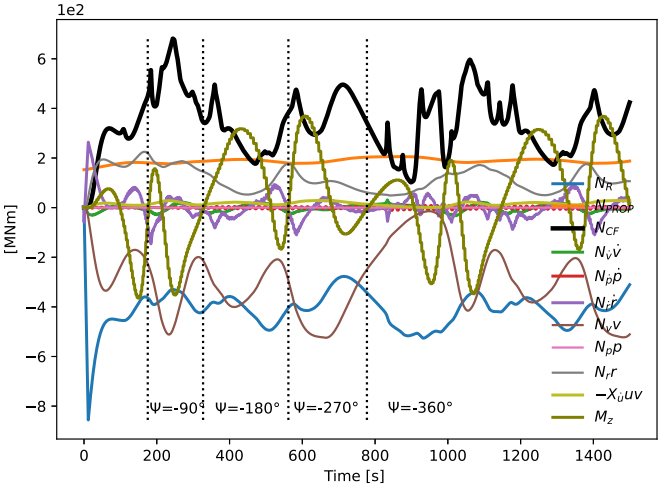

Fig. 28. External yaw moments, from a simulation using the $2D + t$ method, during a turning circle with 35° rudder angle towards starboard, in regular waves with wavelength $\lambda/L_{pp} = 0.86$, wave steepness $H/\lambda = 1/40$, and initial head sea. The approach speed is 11.23 knots (Fn = 0.1). Time instants for heading $\Psi = -90°$, $-180°$, $-270°$, and $-360°$ are indicated.

step-wise behavior of the second order drift loads is due to the fact that these loads are updated at a more slowly varying time-scale than the rest of the loads (here at $\Delta\Psi = 2°$ or $\Delta u = 0.2$ m/s).

Tactical diameter and advance for turning circles with 35° and 25° rudder angle towards starboard are presented in Figs. 29–32, for calm water conditions and for regular waves with relative wavelength $\lambda/L_{pp} = 0.281$, 0.438, 0.630, 0.858, and 1.120, with wave steepness $H/\lambda = 1/40$. For the 35° turning circle, one extra wavelength, $\lambda/L_{pp} = 0.528$, is included. In the experiments, the propeller RPS was the same for all conditions, corresponding to a Froude number $Fn = 0.14$ in calm water. The approach velocity in the numerical simulations are identical to the experimental velocity. 95% confidence intervals, based on repetition tests, are indicated with error bars for the experimental results with relative wavelength $\lambda/L_{pp} = 0.438$ and 0.86. Between three and five repetitions were performed for the different conditions. The 95% confidence intervals are calculated according to ITTC (2014), more information about the repeatability analysis can be found in Rabliås and Kristiansen (2019).

Considering the tactical diameter and advance for the turning circles with 35° rudder angle, presented in Figs. 29 and 30, both 2D+t methods and the cross-flow approach follows the same trend as the experimental results, with decreasing values with increasing wavelength. Overall, both the tactical diameter and the advance is better represented with the $2D+t$ method compared with the cross-flow method and the $2D+t^{cyl}$ method. This is consistent with the observations in Figs. 18 and 22. The tactical diameter simulated with the $2D + t$ method is within 20.1% of the experimental results for all wavelengths. The largest deviation is observed for $\lambda/L_{pp} = 0.63$. Considering this you can have in mind that the DTC hull has a pitch resonance around wavelength $\lambda/L_{pp} = 0.5$ and a heave resonance around wavelength $\lambda/L_{pp} = 0.63$. The exact resonance wavelengths will of course vary with the heading and forward speed, but for the investigated maneuvers they will be close to these wavelengths. The advance is within 2.6% of the experimental

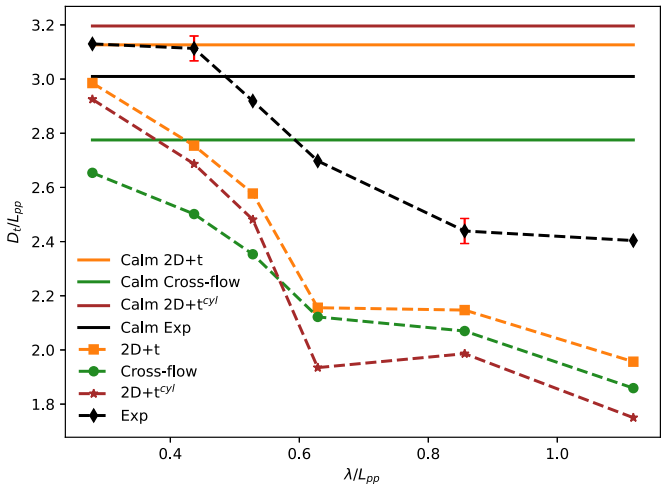

Fig. 29. Tactical diameter of turning circles of the DTC hull with 35° rudder angle towards starboard. Calm water and regular waves with wave steepness $H/\lambda = 1/40$. Simulations where the transverse viscous loads are calculated with pure cross-flow, $2D+t$, and $2D+t^{cyl}$ are presented. 95% confidence intervals, based on repetition tests, are indicated with error bars for the experimental results with relative wavelength $\lambda/L_{pp} = 0.438$ and 0.86.

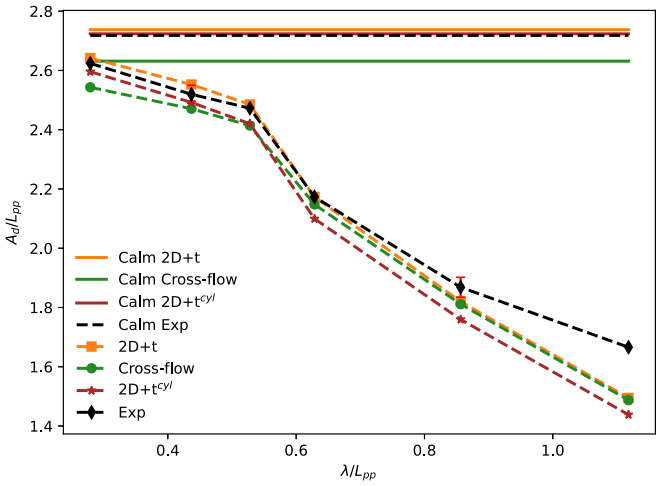

Fig. 30. Advance of turning circles of the DTC hull with 35° rudder angle towards starboard. Calm water and regular waves with wave steepness $H/\lambda = 1/40$. Simulations where the transverse viscous loads are calculated with pure cross-flow, $2D+t$, and $2D+t^{cyl}$ are presented. For calm water, the $2D+t^{cyl}$ method predicts exactly the same advance as the experimental results. 95% confidence intervals, based on repetition tests, are indicated with error bars for the experimental results with relative wavelength $\lambda/L_{pp} = 0.438$ and 0.86.

results for all wavelengths, except for wavelength $\lambda/L_{pp} = 1.120$, which is almost within the stochastic uncertainty of the experiments indicated with the error bars. Wavelength $\lambda/L_{pp} = 1.120$ stands out, where the advance is 10.3% lower than the experimental value.

For the turning circles with 25° rudder angle, presented in Figs. 31 and 32, the tactical diameter and advance in calm water are better represented with the cross-flow principle. In regular waves, the tactical diameter is better represented with the $2D+t$ method. We observe the same as for the 35° turning circle, that the deviation from the experimental results is largest close to heave resonance at wavelength $\lambda/L_{pp} = 0.63$, where the deviation is 10.04%. For the advance the three methods follow each other closely for the investigated range of wavelengths.

For turning circles in waves, one should be careful to conclude by considering the tactical diameter and advance only. The circle can be significantly deformed due to the wave environment, and you can get drifting patterns which not are captured by these standard parameters, i.e you can get a very good match for the advance and tactical diameter while the trajectory can deviate significantly at a later stage in the maneuver. However, since the main objective of this work is to compare different methods to estimate the transverse viscous loads, the tactical diameter and advance can be appropriate indicators to consider the performance of the methods.

5. Conclusion

Simulations in calm water and regular waves are performed with three different methods for the transverse viscous loads; one based on the cross-flow assumption, and the two others based on the 2D+t approach. The $2D+t^{cyl}$ method use scaled time-varying drag coefficients for a circular cylinder, while the $2D+t$ method time-integrates the drag coefficients along the hull with time-derivatives from ship sections in the literature. Since different methods perform best for different maneuvers, it is difficult to definitely conclude which method that estimates the transverse viscous loads most accurately. Overall, considering turning circles with 25° and 35° rudder angles in calm water and regular waves, the $2D+t$ method with integrated drag coefficients is slightly better than the other methods. This is a more sophisticated method compared to the cross-flow principle and the $2D+t^{cyl}$ method. The cross-flow method is more straight-forward to implement, and performs acceptably for the tested maneuvers. Considering 2D+t, using scaled drag coefficients for a circular cylinder can be a good starting point, especially in calm water with drift angles below 25°.

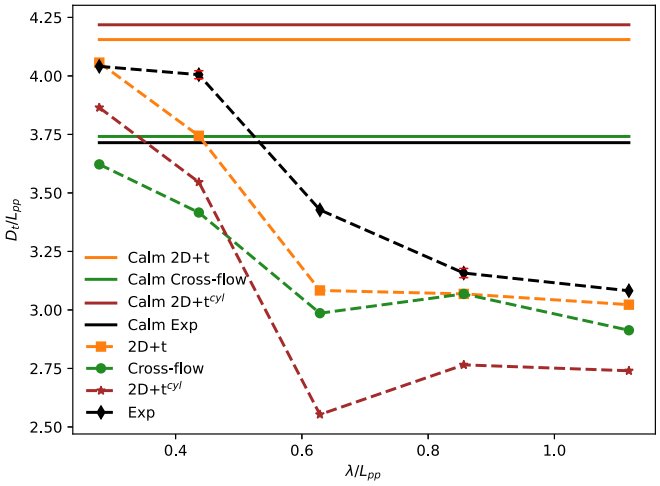

Fig. 31. Tactical diameter of turning circles of the DTC hull with 25° rudder angle towards starboard. Calm water and regular waves with wave steepness $H/\lambda = 1/40$. Simulations where the transverse viscous loads are calculated with pure cross-flow, $2D+t$, and $2D+t^{cyl}$ are presented. 95% confidence intervals, based on repetition tests, are indicated with error bars for the experimental results with relative wavelength $\lambda/L_{pp} = 0.438$ and 0.86.

CRediT authorship contribution statement

Øyvind Rabliås: Conceptualization, Methodology, Investigation, Data curation, Formal analysis, Software, Writing - original draft, Writing - review & editing. **Trygve Kristiansen:** Conceptualization, Formal analysis, Methodology, Writing - review & editing.

Declaration of competing interest

The authors declare that they have no known competing financial interests or personal relationships that could have appeared to influence the work reported in this paper.

Acknowledgments

This work was financed by internal NTNU funds, and by the Research Council of Norway, NFR project 237929 SFI Moove.

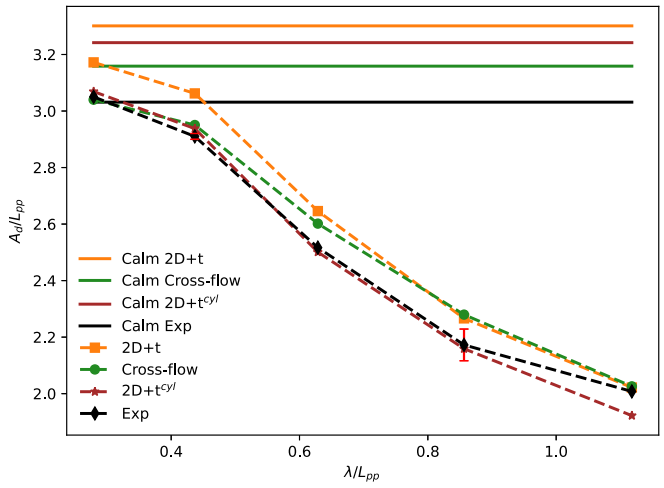

Fig. 32. Advance of turning circles of the DTC hull with 25° rudder angle towards starboard. Calm water and regular waves with wave steepness $H/\lambda = 1/40$. Simulations where the transverse viscous loads are calculated with pure cross-flow, $2D + t$, and $2D+t^{cyl}$ are presented. 95% confidence intervals, based on repetition tests, are indicated with error bars for the experimental results with relative wavelength $\lambda/L_{pp} = 0.438$ and 0.86.

References

Aarsnes, J.V., 1984. Current forces on ships. In: Rapport (Norges tekniske høgskole. Marinteknisk avdeling) (trykt utg.), vol. UR-84-39, Division of Marine Hydrodynamics, Norwegian Institute of Technology, University of Trondheim, Trondheim.

Alsos, H.S., Faltinsen, O.M., 2018. 3D motion dynamics of axisymmetric bodies falling through water. Ocean Eng. 169, 442–456. http://dx.doi.org/10.1016/j.oceaneng.2018.08.033.

Arslan, T., Pettersen, B., Andersson, H.I., 2016. Large-eddy simulation of cross-flow around ship sections. J. Mar. Sci. Technol. 21 (3), 552–566. http://dx.doi.org/10.1007/s00773-015-0366-6, Copyright - JASNAOE 2016.

Artyszuk, J., 2003. A look into motion equations of the 'Esso Osaka' manoeuvring. Int. Shipbuild. Prog. 50 (4), 297–315.

Bertram, V., 2000. Practical Ship Hydrodynamics. Oxford: Elsevier Science & Technology, Oxford.

Brix, J., 1993. Manoeuvring Technical Manual. Seehafen Verlag, Hamburg.

Chapman, R., 1975. Free surface effects for hydrodynamic forces on a surface-piercing plate oscillating in yaw and sway. In: Proceedings of 1st International Conference on Numerical Ship Hydrodynamics, pp. 333–350.

Chillcce, G., el Moctar, O., 2018. A numerical method for manoeuvring simulation in regular waves. Ocean Eng. 170, 434–444. http://dx.doi.org/10.1016/j.oceaneng.2018.09.047.

Cura-Hochbaum, A., Uharek, S., 2016. Prediction of ship manoeuvrability in waves based on RANS simulations. In: 31st Symposium on Naval Hydrodynamics.

Faltinsen, O.M., 1990. Sea Loads on Ships and Offshore Structures. In: Cambridge Ocean Technology Series, Cambridge University Press, Cambridge.

Faltinsen, O.M., 2005. Hydrodynamics of High-Speed Marine Vehicles. Cambridge University Press.

Faltinsen, O.M., Minsaas, K.J., Liapis, N., Skjørdal, S.O., 1980. Prediction of resistance and propulsion of a ship in a seaway. In: Proceedings of the 13th Symposium on Naval Hydrodynamics, Tokyo, 1980.

Faltinsen, O.M., Sortland, B., 1987. Slow drift eddy making damping of a ship. Appl. Ocean Res. 9 (1), 37–46. http://dx.doi.org/10.1016/S0141-1187(87)80001-9.

Fujii, H., 1975. Experimental study on the resistance increase of a ship in regular oblique waves. In: Proc. of 14th ITTC, 1975, Vol. 4, pp. 351–360.

Guo, B., Steen, S., 2010. Added resistance of a VLCC in short waves. In: Proceedings of the ASME 2010 29th International Conference on Ocean, Offshore and Arctic Engineering, Vol. 3. pp. 609–617. http://dx.doi.org/10.1115/OMAE2010-20115.

Hamel-Derouich, D., 1993. Hydrodynamic forces on rectangular cylinders horizontally submerged in waves and currents at low KC numbers. In: Proceedings of the Third International Offshore and Polar Engineering Conference. pp. 168–175, URL: https://www.scopus.com/inward/record.uri?eid=2-s2.0-0027239068&partnerID=40&md5=2495128ee30f04079f5c0a1b00ae13d4.

Hoerner, S.F., 1965. Fluid-Dynamic Drag : Practical Information on Aerodynamic Drag and Hydrodynamic Resistance, third ed. S.F. Hoerner, Midland Park, N.J.

Hooft, J.P., 1994. The cross-flow drag on a manoeuvring ship. Ocean Eng. 21 (3), 329–342. http://dx.doi.org/10.1016/0029-8018(94)90004-3.

Ikeda, Y., 2004. Prediction methods of roll damping of ships and their application to determine optimum stabilization devices. Mar. Technol. SNAME News 41 (2), 89–93.

Ikeda, Y., Himeno, Y., Tanaka, N., 1978. Components of Roll Damping of Ship at Forward Speed, Vol. 404. The Department, Osaka.

ITTC, 2014. Uncertainty Analysis for Free Running Model Tests. Report, ITTC-Recommended Procedures and Guidelines.

Kinaci, O.K., Sukas, O.F., Bal, S., 2019. A modular mathematical approach to predict the maneuvering ability of duisburg test case in regular waves. In: 5th MASHCON: International Conference on Ship Manoeuvering in Shaollow and Confined Water with Non-Exclusice Focus on Manoeuvering in Waves, Wind and Current, pp. 252–264.

Landrini, M., Campana, E.F., 1996. Steady waves and forces about a yawing flat plate. J. Ship Res. 40 (03), 179–192.

Mercier, R.S., Huijs, F.A., 2005. Steady current forces on tanker-based FPSOs. In: WIT Transactions on the Built Environment, Vol. 84. pp. 259–268, URL: https://www.scopus.com/inward/record.uri?eid=2-s2.0-77949760041&partnerID=40&md5=63f989ca8d2b18b5c86eb80181ec3fc2.

el Moctar, O., Shigunov, V., Zorn, T., 2012. Duisburg test case: Post-panamax container ship for benchmarking. Ship Technol. Res. 59 (3), 50–64. http://dx.doi.org/10.1179/str.2012.59.3.004.

Ogawa, A., Koyama, T., Kijima, K., 1977. MMG report-I, on the mathematical model of ship manoeuvring. Bull. Soc. Naval Archit. Jpn. 575 (22–28).

Oltmann, P., Sharma, S.D., 1984. Simulation of combined engine and rudder maneuvers using an improved model of hull-propeller-rudder interactions. In: 15th Symposium on Naval Hydrodynamics. pp. 1–24. http://dx.doi.org/10.15480/882.929.

Ommani, B., Faltinsen, O.M., 2014. Cross-flow transverse force and yaw moment on a semi-displacement vessel with forward speed and drift angle. In: Proceedings of the 11th International Conference on Hydrodynamics, ICHD.

Ommani, B., Faltinsen, O.M., Lugni, C., 2012. Hydrodynamic forces on a semi-displacement vessel on straight course with drift angle. In: 10th International Conference on Hydrodynamics, ICHD, Vol. 2, pp. 243–250.

Rabliås, Ø., Kristiansen, T., 2019. Free running maneuvering tests of the dtc hull in calm water and regular waves with focus on uncertainty analysis based on repetition tests. In: 5th MASHCON: International Conference on Ship Manoeuvering in Shaollow and Confined Water with Non-Exclusice Focus on Manoeuvering in Waves, Wind and Current. pp. 328–339.

Salvesen, N., Tuck, E.O., Faltinsen, O.M., 1970. Ship motions and sea loads. Trans. SNAME 78 (8), 250–287.

Sarpkaya, T., 1966. Separated flow about lifting bodies and impulsive flow about cylinders. AIAA J. 4 (3), 414–420. http://dx.doi.org/10.2514/3.3453.

Sarpkaya, T., Storm, M., 1985. In-line force on a cylinder translating in oscillatory flow. Appl. Ocean Res. 7 (4), 188–196. http://dx.doi.org/10.1016/0141-1187(85)90025-2.

Shen, Y., 2018. Operational Limits for Floating-Collar Fish Farms in Waves and Current, Without and with Well-Boat Presence (Thesis). Avhandling (ph.d.) - Norges teknisk-naturvitenskapelige universitet, Institutt for marin teknikk, Trondheim, 2018.

Shen, Y., Greco, M., Faltinsen, O.M., 2019. Numerical study of a well boat operating at a fish farm in long-crested irregular waves and current. J. Fluids Struct. 84, 97–121. http://dx.doi.org/10.1016/j.jfluidstructs.2018.10.007.

Shigunov, V., El Moctar, O., Papanikolaou, A., Potthoff, R., Liu, S., 2018. International benchmark study on numerical simulation methods for prediction of manoeuvrability of ships in waves. Ocean Eng. 165, 365–385. http://dx.doi.org/10.1016/j.oceaneng.2018.07.031.

Skejic, R., 2008. Maneuvering and Seakeeping of a Single Ship and of Two Ships in Interaction (Ph.d.).

Söding, H., 1982. Prediction of ship steering capabilities. Schiffstechnik 29, 3–29.

Sprenger, F., Fathi, D., 2015. D3.3 Report on Model Tests at MARINTEK. Report SHOPERA-D3.3, URL: http://shopera.org/public-documents/.

Sutulo, S., Soares, C.G., 2011. Mathematical models for simulation of manoeuvring performance of ships. Mar. Technol. Eng. 661–698, URL: https://www.scopus.com/inward/record.uri?eid=2-s2.0-84864050719&partnerID=40&md5=8fde7aff1b7d02d4b7ec9acdf7bc0a3e.

Sutulo, S., Soares, C.G., 2019. On the application of empiric methods for prediction of ship manoeuvring properties and associated uncertainties. Ocean Eng. 186, 106–111. http://dx.doi.org/10.1016/j.oceaneng.2019.106111.

Tanaka, N., 1983. Hydrodynamic viscous force acting on oscillating cylinders with various shapes. In: Osaka University, Department of Naval Architecture, Report No. 407, 6th Symposium of Marine Technology of the Society of Naval Architects of Japan, 1982.

Tello Ruiz, M., 2018. Manoeuvring Model of a Container Vessel in Coastal Waves (Thesis).

Wicaksono, A., Kashiwagi, M., 2018. Wave-induced steady forces and yaw moment of a ship advancing in oblique waves. J. Mar. Sci. Technol. 23 (4), 767–781. http://dx.doi.org/10.1007/s00773-017-0510-6.

Yasukawa, H., Yoshimura, Y., 2015. Introduction of MMG standard method for ship maneuvering predictions. J. Mar. Sci. Technol. 20 (1), 37–52. http://dx.doi.org/10.1007/s00773-014-0293-y.

Yeung, R.W., Seah, R.K.M., Imamura, J.T., 2008. Separated flow about a slender body in forward and lateral motion. In: ASME 2008 27th International Conference on Offshore Mechanics and Arctic Engineering, Vol. 4: Ocean Engineering; Offshore Renewable Energy. pp. 349–359. http://dx.doi.org/10.1115/omae2008-57480.